Journal of South American Earth Sciences 78 (2017) 38–60

Contents lists available at ScienceDirect

Journal of South American Earth Sciences

journal homepage: www.elsevier.com/locate/jsames

The Palaeocene Cerro Munro tonalite intrusion (Chubut Province, Argentina): A plutonic remnant of explosive volcanism?

C. Rodríguez [a, *], E. Aragón [b, e], A. Castro [a], R. Pedreira [c], A. Sánchez-Navas [d], J. Díaz-Alvarado [f], F. D'Eramo [g], L. Pinotti [g], Y. Aguilera [e], C. Cavarozzi [e], M. Demartis [g], I.R. Hernando [b, e], T. Fuentes [b, e]

[a] Departamento de Ciencias de la Tierra, Universidad de Huelva, Campus El Carmen, 21071 Huelva, Spain
[b] Facultad de Ciencias Naturales y Museo (UNLP), 122 y 60, s/n. (1900), La Plata, Buenos Aires, Argentina
[c] Département des sciences appliquées, Unité d'enseignement en sciences de la Terre, 555 Boulevard de l'Université (G7H 2B1), Chicoutimi, Québec, Canada
[d] Departamento de Mineralogía y Petrología, Universidad de Granada, Spain
[e] Centro de Investigaciones Geológicas, UNLP-CONICET, Calle 1 N° 644 (1900), La Plata, Argentina
[f] Departamento de Geología, Universidad de Atacama, Copayapu 485, Copiapó, Chile
[g] Departamento de Ciencias Geológicas, UNRIV, Río Cuarto, Argentina

ARTICLE INFO

Article history:
Received 21 February 2017
Accepted 7 June 2017
Available online 10 June 2017

Keywords:
Calc-alkaline magmatism
Tonalites
Autoliths
Fractionation
Cathodoluminiscence

ABSTRACT

The Cerro Munro sub-volcanic intrusion is emplaced in the back-arc (400 km from the trench) as small sub-circular tonalite-granodiorite plutons with abundant radial porphyritic dikes. U-Pb zircon SHRIMP data give an age of crystallization of 57 Ma ± 1.4 Ma. It is located to the east of the North Patagonian Batholith (NPB) that shows a protracted and episodic magmatic history from Cretaceous to Miocene time. The NPB Palaeogene episode is characterized by the lack of magmatic activity at the arc axis, as small plutonic emplacements move to the fore-arc and back-arc. This Palaeogene tectono-magmatic episode is ruled by the detachment of the Aluk plate during the Aluk-Farallon-SAM triple junction, active at that time along northern Patagonia active margin, changing the Cretaceous "NPB orogenic" setting to a Palaeogene "Munro transitional" tectono-magmatic setting. Near the contacts, the tonalite contains abundant enclaves of igneous appearance and variable size from several cm to dm, described as autoliths. The study of autoliths and host tonalite reveals interesting results on the processes of fractionation in a thermally zoned magma chamber. Autoliths, and in a large extent the host tonalite, represent disguised cumulates from which a hydrous silicic liquid was extracted. Barometry calculations from mineral chemistry in both autoliths and tonalites record a shallow pressure of emplacement of 0.5 kbar. Rhyolite-dacite flows and ignimbrites, surrounding the northern contact of the Cerro Munro tonalite, may represent the exsolved liquid from the plutonic cumulates. The study by cathodoluminiscence and electron backscattered diffraction techniques from a rhyolite-hosted quartz supports this protracted history of the Cerro Munro magma chamber.

1. Introduction

The connection between volcanic and plutonic rocks is nowadays subject of discussion due to their implications in understanding deep-seated processes observed in magmatic rocks (Bachmann and Bergantz, 2004, 2008; Bachmann et al., 2007; Deering et al., 2016; Frost et al., 2016; Gelman et al., 2014; Glazner et al., 2008; Lipman and Bachmann, 2015). Recently, granites have been described as cumulate rocks formed by crystallization and expulsion of an interstitial liquid (Lee and Morton, 2015; Vernon and Collins, 2011). Many felsic plutons have been interpreted as the potential residues of rhyolitic eruptions (Bachmann and Bergantz, 2004, 2008; Deering and Bachmann, 2010). The retained liquid in the cumulate corresponds only to the terminal porosity (20–30% (Donev et al., 2004), and consequently, it can be difficult to recognize cumulate features in these rocks, except for the textures (Lee and Morton, 2015). Because of the high viscosity of silicic systems and its consequent inability to

* Corresponding author.
E-mail address: carmen.rodriguez@dgeo.uhu.es (C. Rodríguez).

http://dx.doi.org/10.1016/j.jsames.2017.06.002
0895-9811/

expel the interstitial liquid by gravity forces (Glazner, 2014), the melt-segregation remains obscure. Water decreases the viscosity of melts, and bubbles can favour its mobility allowing the residual liquid expulsion in these silicic magma chambers or ascent conduits (Boudreau, 2016; Lee et al., 2015; Pistone et al., 2015).

The North Patagonian Batholith (NPB) is an excellent example to study magmatic processes regarding the volcanic-plutonic connection. The NPB shows a protracted and episodic magmatic history from Cretaceous to Miocene time. The NPB Palaeogene episode is characterized by the lack of magmatic activity at the arc axis, as small plutonic emplacements move to the fore-arc and back-arc. This Palaeogene episode is ruled by the detachment of the Aluk plate during the Aluk-Farallon-SAM triple junction development along northern Patagonia, changing the "orogenic" setting to a "transitional" tectono-magmatic one. The Cerro Munro tonalite is an 8 km diameter, lens-shaped body intruding into Carboniferous-Permian sediments from the Tepuel Group (Lower Jurassic) and is surrounded by silicic volcanic and volcaniclastic rocks at its northern boundary. This tonalitic body is characterized by the presence of abundant enclaves with variable shapes varying from irregular and angular to rounded, the smallest ones showing the more rounded shape. The tonalite shows coarse-grained texture and its enclaves have finer grain size.

Here we show a geochemical and petrological characterization for the Cerro Munro magmatic system and we investigate the possible implications on calc-alkaline magmatism. As a whole, the Cerro Munro intrusion is zoned and ranges from dioritic to tonalitic compositions from east to west. Geochemical trends of the tonalite and enclaves follow typical calc-alkaline patterns. Paired samples of enclaves and host tonalites were collected in order to discriminate between local- and pluton-scale processes of magma fractionation. The study of these rocks reveals interesting results on the processes of magma differentiation in thermally zoned magma chambers or ascent conduits. Enclaves and, to a large extent, the host tonalite, represent disguised cumulates from which a hydrous silicic liquid was extracted, while rhyolite-dacite flows and ignimbrites hosting the Cerro Munro tonalite, may represent the exsolved liquid from the plutonic cumulates.

Detailed observation of igneous textures are key factors in recognizing the "missing" cumulates, needed to generate silicic plutons (Lee and Morton, 2015). Complementary tools to address this problem as geochemical modelling can be useful to clarify the process accounting for silicic differentiation, as *in-situ* crystallization (Langmuir, 1989; Lee and Morton, 2015).

On the other hand, cathodoluminiscence techniques in quartz found in volcanic and plutonic rocks have clearly proved to be useful in recording magmatic processes as rejuvenation, mingling and recharge of magma chambers (Beane and Wiebe, 2012; D'Lemos et al., 1997; Matthews et al., 2011, 2012; Wiebe et al., 2007). Here we show the recorded history in volcanic quartz of the Cerro Munro magma chamber, directly related to the plutonic counterparts in this work.

2. Geological setting

Further east of the Patagonian Andes, several small size plutons (5–10 km diameter) known as the Munro, Menucos, Tepuel and Kanquel plutons with upper Cretaceous-Palaeocene K-Ar age, have been mapped as Aleusco Formation (Turner, 1982). The original work of Turner (1982) included the outcrops of the Aleusco locality, which now are known to be of early Jurassic age (Haller et al., 1999; Rapela et al., 2005). Since the denomination of Aleusco is now used to describe the early Jurassic granitoids of the area (Haller et al., 1999; Rapela et al., 2005) and correlate this unit to the Jurassic Subcordilleran plutonic belt, we preferred to use the denomination of Cerro Munro system to describe the Palaeocene granitic rocks of this area, to avoid any confusion.

The plutonic rocks from the Cerro Munro intrude Carboniferous-Permian sediments of Tepuel Group, lower Jurassic sediments of the Lepá Formation, Granitoids of the early Jurassic Subcordilleran plutonic belt (Haller et al., 1999; Rapela et al., 2005), and Gabbros of the Tecka Formation (Turner, 1982). In turn, they are intruded and covered by volcanic rocks of the Cautiva Complex (Spikermann, 1978; Turner, 1982). La Cautiva Complex volcanic rocks that intrude the Menucos Pluton have a K/Ar age of 54 ± 3 Ma (Turner, 1982). The Cautiva Complex on the regional context is included in the Eastern Palaeocene Volcanic belt (EPEB) (Rapela et al., 1987). Most radiometric K/Ar ages of the EPEB range from 60 to 42 Ma (Rapela et al., 1983). The EPEB is a bimodal volcanism rhyolite-basalt, where rhyolites and dacites predominate as large ignimbrite plateaux and subordinate domes and lava flows (Aragón and Mazzoni, 1997; Rapela et al., 1987), suggesting an ignimbrite flare-up. The basalts are tholeiitic and alkalic (Aragón et al., 2011). To the west of the EPEB a second and younger volcanic belt known as Western Oligocene Volcanic belt (WOB) define a typical calc-alkaline association (Fig. 1; Rapela et al., 1983, 1987). The WOB volcanic rocks also start as dacite-rhyolite flows and ignimbrites. The top of the sequence is mostly andesitic to basaltic, and shows a range of K/Ar radiometric ages of 24–33 Ma (Rapela et al., 1987). Coeval to the WOB but on the former fore-arc is the Coastal Volcanic belt (CVB; Muñoz et al., 2000) having basalts of primitive composition.

Both volcanic belts (EPEB and WOB) have late basaltic flows with OIB affinity (Aragón et al., 2005; Kay and Rapela, 1987), and are the eastern and western boundaries of the Ñirihuau basin (Cazau et al., 1989; Spalletti, 1983). The extent of the extensional tectonic setting with the development of fore-arc, arc and back-arc basins reached its maximum in the Oligocene (Giacosa and Heredia, 2004; Jordan et al., 2001; Mancini and Serna, 1989; Rapela et al., 1983, 1987; Silvestro and Zubiri, 2008).

To the west of the Cerro Munro system, and running along the main cordillera of the Patagonian Andes is the North Patagonian batholith (Fig. 1). This large magmatic system shows a protracted and episodic plutonic activity with a complex distribution (Pankhurst et al., 1999). These authors used detailed Rb-Sr geochronology to show that plutonic emplacement spanned from 140 Ma to 9 Ma. The age's distribution show that plutonism is episodic, having a severe decrease of plutonism during the Palaeogene, besides, the few plutons are Eocene and migrated to the west of the main mid-Cretaceous batholith axis, constrained to the major Liquiñe-Ofqui fault zone. Finally, the continuous plutonic emplacement in the arc axis is recovered in the Miocene, but these magmas are relatively primitive in terms of their isotopic composition.

The South Patagonian batholith (Hervé et al., 2007) has a similar time-space zonation and geochemical evolution with respect to the North Patagonian batholith.

Aragón et al., 2011 showed that for the Palaeogene time, the southward migration of the Farallon-Aluk-SAM triple junction with a highly oblique Farallon plate convergence, has unzipped the subducted Aluk plate, developing a transform plate margin with a slab-window as the Aluk plate was detached. This situation has also been proposed to explain the NPB, EPEB, WOB and CVB time-space distribution changes. From this perspective, the tectono-magmatic setting of the typical Cretaceous and Miocene NPB magmatism is "*Orogenic*". Instead the Palaeogene igneous episodes in the NPB, EPEB, WOB and CVB are considered to be "*Transitional*" between the "*Orogenic*" and "*Within Plate*" tectono-magmatic settings.

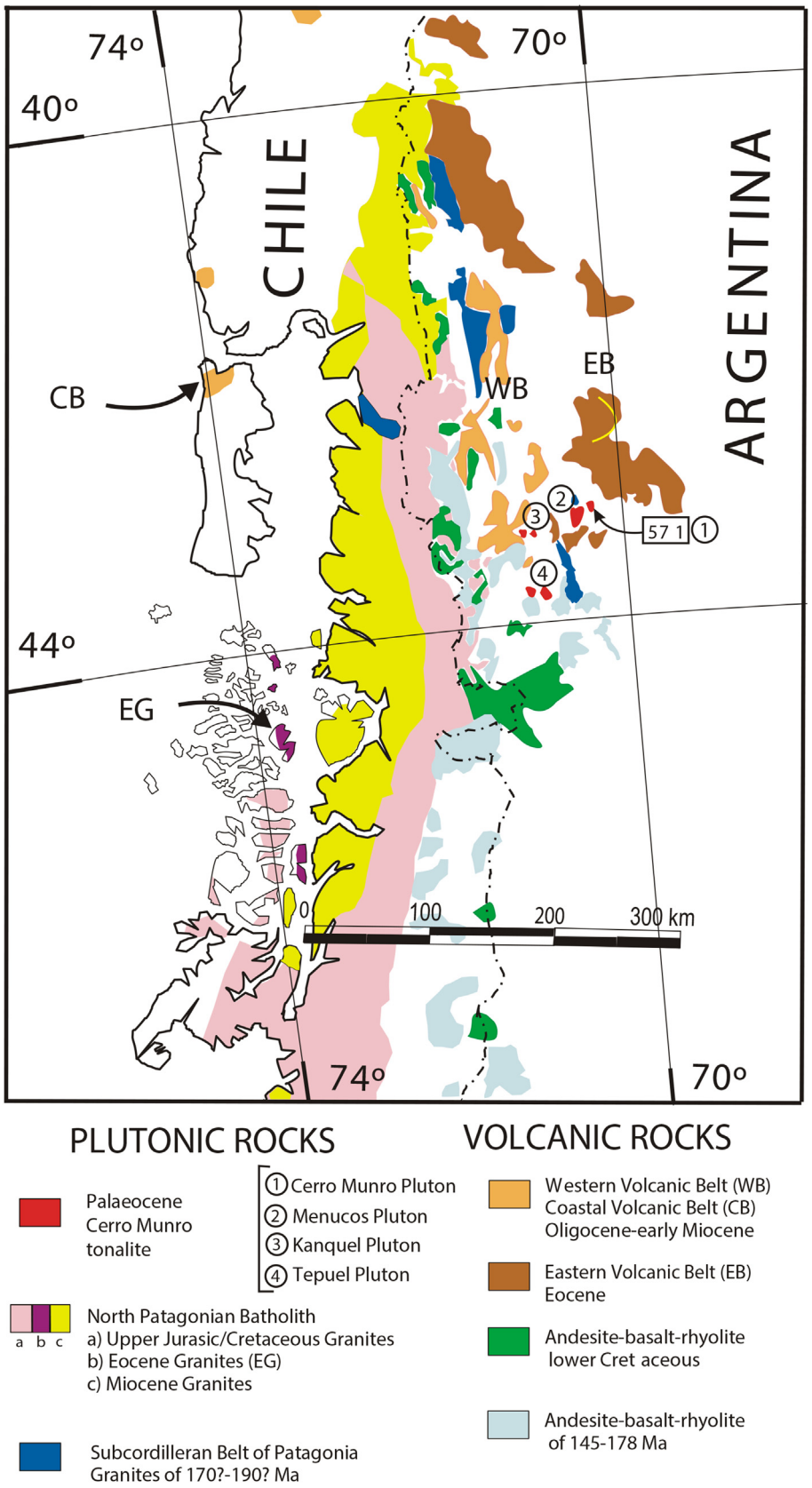

Fig. 1. Location map of northern Patagonia, showing the major igneous units related to the active margin from the Jurassic to the Cenozoic. Numbered circles provide the location for post-tectonic Palaeocene plutons. The NPB time-space distribution is modified from Pankhurst et al. (1999).

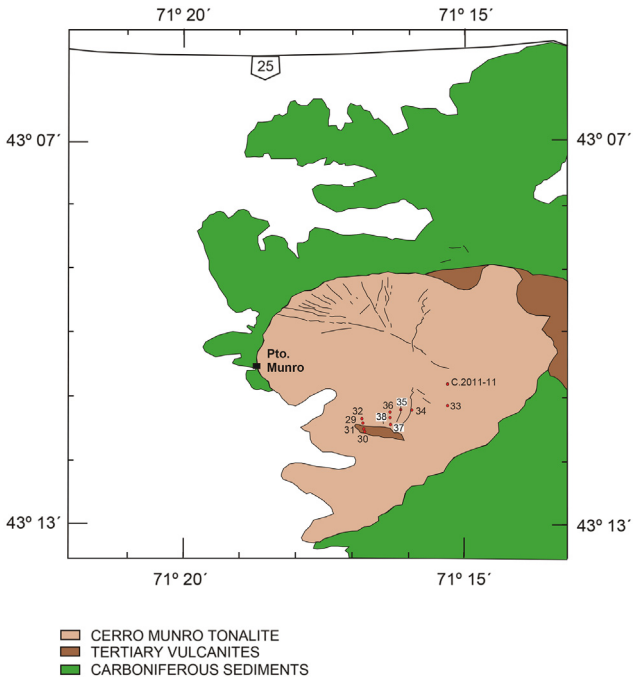

Fig. 2. Geological map of Cerro Munro tonalite with location of the collected samples.

3. The Cerro Munro tonalite

The Cerro Munro body is made of Palaeocene epizonal granitic rocks. In the original description, these palaeocene plutonic rocks are included in the Aleusco batholith (Spikermann et al., 1988, 1989). These authors recognized two plutonic episodes: a main phase to the north and a late phase to the south. Although Spikermann et al. (1988), obtained a Jurassic age (K/Ar) for the northern Main plutonic phase, they rejected this age in favour of the more frequent Palaeocene ages (K/Ar ages; Spikermann, 1978; Turner, 1982) of the Late plutonic phase in the southern outcrops. Recent K/Ar ages (Haller et al., 1999) and U/Pb SHRIMP zircon ages (Rapela et al., 2005) have demonstrated the northern Main plutonic phase belongs to the Jurassic age and these authors have reassigned the Aleusco Formation to the Jurassic and correlated the granitoids to the Jurassic Subcordilleran belt. Therefore, in this paper we introduce the denomination of Cerro Munro system for the Palaeocene southern granitoid outcrops (Fig. 1).

The Cerro Munro tonalite has pale grey to pink medium grained rocks that comprise granodiorites/quartz-monzodiorites with subordinate tonalites/diorites and granites. The plutons have abundant round dark inclusions of a fine grain size (mafic-rich enclaves), irregular patches and dikes of micro-leucogranites (graphic and miarolitic), dikes of aplites, and abundant porphyritic dikes of andesitic and rhyolitic composition arranged in radial geometry.

The detailed study of the example of Cerro Munro intrusion (listed as 1 in Fig. 1) is exposed in this work. The emplacement structure is well exposed. This is a sub-circular body with a major

Fig. 3. Field relations between tonalites and autoliths from Cerro Munro body. (a) Outcrop of autoliths within the tonalite A312-37. (b) Rounded microgranular autolith of dm-size hosted in the coarse-grained tonalite A312-33. (c) Coarse-grained texture of the tonalite A312-32. (d) Fine-grained texture of the autoliths.

Table 1
Whole-rock analyses of major and trace elements of Cerro Munro pluton and related host-rocks.

Sample	A312-29	A312-29b	A312-32	A312-33	A312-33a-g	A312-36	A312-36a	A312-36b	A312-36c	A312-37	A312-37a	A312-38	C.2011-11	A312-30	A312-31	A312-34	A312-35
Rock Type	Tonalite	Autolith	Tonalite	Tonalite	Autolith	Tonalite	Autolith	Autolith	Autolith	Tonalite	Autolith	Autolith	Tonalite	Andesite tuff (host rock)	Dacite tuff (host rock)	Rhyolitc porphyry	Andesite porphyry dyke
Major elements (wt%)																	
SiO_2	63.19	57.21	61.95	63.07	57.81	64.21	64.32	61.10	57.86	65.37	57.73	58.31	63.19	60.13	66.44	76.58	61.59
TiO_2	0.80	1.13	0.88	0.79	1.05	0.37	0.43	0.88	0.80	0.69	1.03	0.92	0.80	1.01	0.81	0.04	0.87
Al_2O_3	16.36	16.50	16.51	16.66	16.78	18.92	18.54	16.78	16.81	15.90	16.39	16.73	16.36	17.63	15.55	13.57	16.14
FeOt	4.45	6.68	4.84	4.28	6.35	2.22	2.29	4.98	6.37	3.77	6.27	6.23	4.49	7.43	5.92	0.50	4.60
MgO	2.44	3.44	2.63	2.13	3.77	1.15	1.14	2.93	4.07	1.92	3.60	3.70	2.44	3.35	2.46	0.26	2.44
MnO	0.09	0.14	0.09	0.09	0.17	0.04	0.05	0.09	0.13	0.07	0.15	0.11	0.09	0.19	0.07	0.02	0.08
CaO	4.05	6.24	4.46	3.99	5.50	4.10	3.98	5.17	6.12	3.14	5.62	6.64	4.05	3.66	1.05	0.20	3.84
Na_2O	4.05	4.10	4.00	4.19	4.24	4.57	4.58	3.93	4.09	4.17	4.44	4.39	4.05	1.95	2.35	1.19	4.13
K_2O	2.01	1.61	1.96	2.20	1.82	2.58	2.56	1.73	1.10	2.56	1.57	1.04	2.01	3.05	2.63	5.61	1.92
P_2O_5	0.28	0.39	0.31	0.26	0.30	0.14	0.14	0.30	0.24	0.22	0.34	0.33	0.28	0.35	0.11	0.06	0.38
Loi	1.19	1.16	1.47	1.36	0.98	0.77	0.98	0.92	1.19	1.13	1.42	0.34	1.19	0.00	1.21	1.65	2.98
Total	98.91	98.60	99.10	99.02	98.77	99.07	99.00	98.81	98.77	98.94	98.56	98.74	98.95	98.75	98.60	99.68	98.97
ASI [a]	1.05	0.87	1.03	1.05	0.92	1.08	1.08	0.99	0.91	1.07	0.89	0.85	1.05	1.43	1.86	1.64	1.08
K/K + Ca [b]	0.23	0.13	0.21	0.25	0.16	0.27	0.28	0.17	0.10	0.33	0.14	0.09	0.23	0.33	0.60	0.94	0.23
#Mg [c]	0.49	0.48	0.49	0.47	0.51	0.48	0.47	0.51	0.53	0.48	0.51	0.51	0.49	0.45	0.43	0.48	0.49
Fe* [d]	0.65	0.66	0.65	0.67	0.63	0.66	0.67	0.63	0.61	0.66	0.64	0.63	0.65	0.69	0.71	0.66	0.65
Trace elements (ppm)																	
Li	36.40	32.78	29.93	28.44	36.37	24.80	17.72	27.80	28.23	29.34	40.45	9.08	36.00	103.75	68.84	75.96	54.44
Sc	12.09	20.62	11.93	10.13	21.48	6.54	5.31	12.47	20.56	9.68	20.45	20.33	12.10	21.32	14.56	2.83	11.37
V	92.62	150.53	93.99	78.76	129.16	66.60	47.74	93.84	137.73	72.19	124.08	147.78	92.60	151.52	101.54	3.37	98.74
Cr	51.77	33.38	46.29	25.21	77.57	34.42	17.98	41.99	87.05	26.67	62.10	64.30	51.80	105.11	75.76	1.86	62.86
Co	30.58	26.81	25.46	25.81	29.66	42.46	21.08	27.48	32.19	25.61	27.88	32.63	30.60	34.92	30.11	15.29	23.51
Ni	34.69	31.77	34.13	20.74	43.68	31.93	19.55	38.84	67.27	26.55	32.44	40.00	34.70	53.17	40.33	4.61	27.24
Cu	37.44	197.13	29.02	22.56	44.75	26.94	18.27	33.34	41.05	18.99	28.65	73.09	37.40	31.34	17.81	1.98	34.62
Zn	73.75	89.21	75.39	73.97	129.04	46.85	34.13	69.10	92.06	64.92	110.63	90.03	73.70	112.41	89.76	19.00	88.34
Ga	18.54	17.89	18.10	18.35	18.99	25.78	18.45	17.81	18.07	18.22	18.40	17.64	18.50	23.13	18.86	17.61	18.61
Rb	58.71	49.07	50.14	58.72	57.79	79.96	58.62	44.81	25.32	60.60	51.81	17.62	58.70	128.95	106.50	158.56	42.67
Sr	384.5	389.3	402.0	345.4	352.9	611.7	462.1	420.5	425.7	281.9	369.9	430.8	384.0	168.8	205.1	21.0	484.7
Y	21.25	26.48	20.74	21.76	40.08	11.17	9.34	18.90	22.15	24.96	30.09	21.93	21.20	38.44	14.56	11.55	17.49
Zr	20.31	21.13	37.60	14.67	21.13	32.70	16.54	18.71	27.11	28.75	20.27	30.16	20.00	63.95	16.57	28.02	143.54
Nb	13.77	17.31	14.29	14.97	21.85	9.52	7.75	12.66	10.32	15.50	15.52	10.63	13.80	14.78	13.86	24.44	11.21
Cs	1.92	1.82	1.71	1.96	2.97	2.03	1.33	1.66	0.86	1.21	2.39	0.90	1.90	11.17	6.64	3.16	3.05
Ba	316.2	202.1	316.4	324.7	266.7	379.3	323.8	258.0	196.1	354.0	192.8	258.2	316.0	536.1	394.2	196.9	401.7
La	27.60	33.45	26.53	29.85	33.42	21.05	16.40	23.42	21.10	30.10	31.05	22.74	27.60	41.38	29.44	4.21	25.68
Ce	59.55	73.22	57.26	61.33	81.08	37.45	31.07	50.18	46.79	67.10	68.37	50.05	59.60	86.23	61.90	10.00	55.47
Pr	7.11	8.70	6.80	7.09	10.51	4.17	3.44	6.06	5.90	8.12	8.35	6.19	7.10	10.43	7.19	1.27	6.71
Nd	26.67	32.88	25.53	26.64	41.01	15.16	12.36	22.97	23.03	31.11	32.05	24.44	26.70	41.80	27.81	4.28	25.56
Sm	5.18	6.43	5.02	5.05	8.54	2.74	2.28	4.52	4.84	6.15	6.67	5.11	5.20	9.14	5.47	1.53	4.97
Eu	1.35	1.55	1.30	1.39	1.74	1.57	1.17	1.24	1.44	1.27	1.62	1.50	1.40	2.01	1.26	0.22	1.37
Gd	4.79	5.89	4.41	4.63	7.89	2.32	1.96	4.06	4.59	5.49	6.13	4.72	4.80	8.50	4.54	1.59	4.41
Tb	0.70	0.87	0.66	0.63	1.25	0.34	0.28	0.60	0.68	0.76	0.94	0.69	0.70	1.20	0.57	0.30	0.63
Dy	3.96	4.91	3.71	3.65	7.16	1.79	1.68	3.38	4.08	4.49	5.36	4.00	4.00	6.74	3.06	2.01	3.39
Ho	0.80	1.02	0.75	0.76	1.55	0.38	0.31	0.67	0.86	0.91	1.12	0.82	0.80	1.38	0.56	0.37	0.66
Er	2.04	2.57	1.98	1.95	4.03	1.01	0.81	1.75	2.18	2.33	2.91	2.11	2.00	3.56	1.32	0.99	1.58
Tm	0.31	0.40	0.31	0.30	0.66	0.18	0.13	0.27	0.34	0.35	0.45	0.32	0.30	0.57	0.21	0.16	0.24
Yb	1.93	2.52	1.85	1.91	4.20	1.02	0.82	1.67	2.10	2.05	2.82	1.99	1.90	3.54	1.31	1.05	1.49

Lu	0.27	0.36	0.27	0.28	0.60	0.15	0.12	0.23	0.29	0.30	0.40	0.28	0.30	0.52	0.20	0.15	0.21	
Hf	0.35	0.74	0.98	0.00	0.80	−0.37	0.15	0.34	0.77	0.00	0.59	0.67	0.40	0.00	0.00	0.95	3.07	
Ta	1.67	1.56	1.36	1.42	2.15	3.27	1.51	1.41	1.28	1.62	1.53	1.30	1.70	1.78	1.86	3.20	1.21	
Pb	7.81	10.66	6.15	8.03	20.38	8.54	7.48	7.18	9.44	9.75	12.18	7.53	7.80	27.84	17.64	7.58	8.76	
Th	6.68	6.52	6.91	9.44	7.57	9.80	7.61	6.23	4.81	8.73	6.59	3.57	7.60	11.20	8.89	2.92	5.55	
U	0.57	0.61	0.76	0.75	1.36	0.97	0.68	0.69	0.71	0.75	0.83	0.87	0.60	2.94	1.59	1.95	1.38	

LOI: Loss of ignition.
[a] ASI = $[Al_2O_3/(Na_2O + K_2O+(CaO-1.67*P_2O_5))]$.
[b] K/(K + Ca) = molar $K_2O/[K_2O + CaO]$.
[c] Mg# = molar MgO/[MgO + FeO].
[d] Fe* = wt% FeOt/[FeOt + MgO].

axis trend of N 35°W, with a diameter of 8 km for the Cerro Munro pluton (Fig. 2). Late stage porphyritic radial dikes are arranged towards the rims of the bodies, but do not cut the surrounding country rocks. The Cerro Munro body shows on the northern side an intrusion of Tertiary sub-volcanic rocks and is cut by basaltic to trachyandesitic dikes. Abundant microgranular of igneous appearance and variable size from several cm to dm and scarce leucocratic enclaves characterize Cerro Munro intrusion (Fig. 3). Henceforth, enclaves are referred as autoliths because of its igneous relation to the Cerro Munro tonalite and their common provenance of a unique magmatic system.

4. Sampling and analytical techniques

Sampling on Cerro Munro body was arranged to cover a wide range of diverse tonalites, its respective autoliths and the volcanic rocks. Autolith shapes vary from irregular and angular to rounded, the smallest showing the more rounded shape (Fig. 3a and b). The tonalite shows coarse-grained texture (Fig. 3c) increasing from the contact inwards and its autoliths have finer grain size (Fig. 3d).

Approximately 3 kg of fresh rock was collected from tonalites and was crushed and milled to a fine powder for whole-rock geochemistry. In the case of autoliths, the entire sample was completely crushed, except fragments for the petrographic study. Major elements were determined by X-ray fluorescence (XRF) at the CIC (University of Granada, Spain). Precision for major elements is better than 1%. Trace elements were obtained by inductively coupled plasma mass spectrometry (ICP-MS) at the University of Granada, following the standard procedures described by Baedecker (1987). Analysis of trace elements was carried out according to the method described by Bea et al. (1996); the precision was approximately 2% and 5% error on concentrations of 50 and 5 ppm, respectively. Thin sections of intrusive samples were polished and subsequently analysed in order to determine the composition of major elements in mineral phases using a JEOL JXA-8200 Superprobe at the University of Huelva (Spain). A combination of silicates and oxides were used for calibration. A defocused beam of 10-μm diameter was used to analyse glasses to minimize Na migration. For the EBSD and cathodoluminiscence study, the sample was cut and polished with silica gel, and subsequently analysed structurally.

5. Whole-rock geochemistry of Cerro Munro intrusive and related volcanic rocks

Seventeen samples of tonalites, related autoliths, porphyry dykes and host rocks were collected in fresh outcrops. Tonalites and autoliths show a silica range from SiO_2 = 57 to 65 wt% (Table 1 and Fig. 4). Both tonalites and autoliths are magnesian and calc-alkalic according to the Peacock index (Fig. 4a and b). Autoliths are metaluminous (Fig. 4c) and have a narrow silica range (SiO_2: 57–58 wt %, except autoliths from A312-36) whilst tonalites are slightly peraluminous. A systematic correlation between autolith-host pairs was found (Fig. 4). Considering the autolith-tonalite pairs separately, there is a marked silica gap about 7 wt% SiO_2 (Fig. 4). The relation of molar ratio $K_2O/(K_2O + CaO)$ vs K_2O (Fig. 5a) of tonalites and autoliths coincides with a typical calc-alkaline trend of Cordilleran batholith. However, Mg# maintains high values as silica content increases (Fig. 5b), moving away from the calc-alkaline differentiation pattern. Preferentially, autoliths have dioritic compositions while their host-rock belongs to the grano-tonalite field (Fig. 5c). Also, in this diagram we can appreciate enrichment in the molar ratio $K_2O/(K_2O + CaO)$ regarding the fractionation trend of Patagonian Batholith. In the Mg# vs MgO (wt%) diagram (Fig. 5d), it can be observed that the flat pattern of the variation of Mg# should

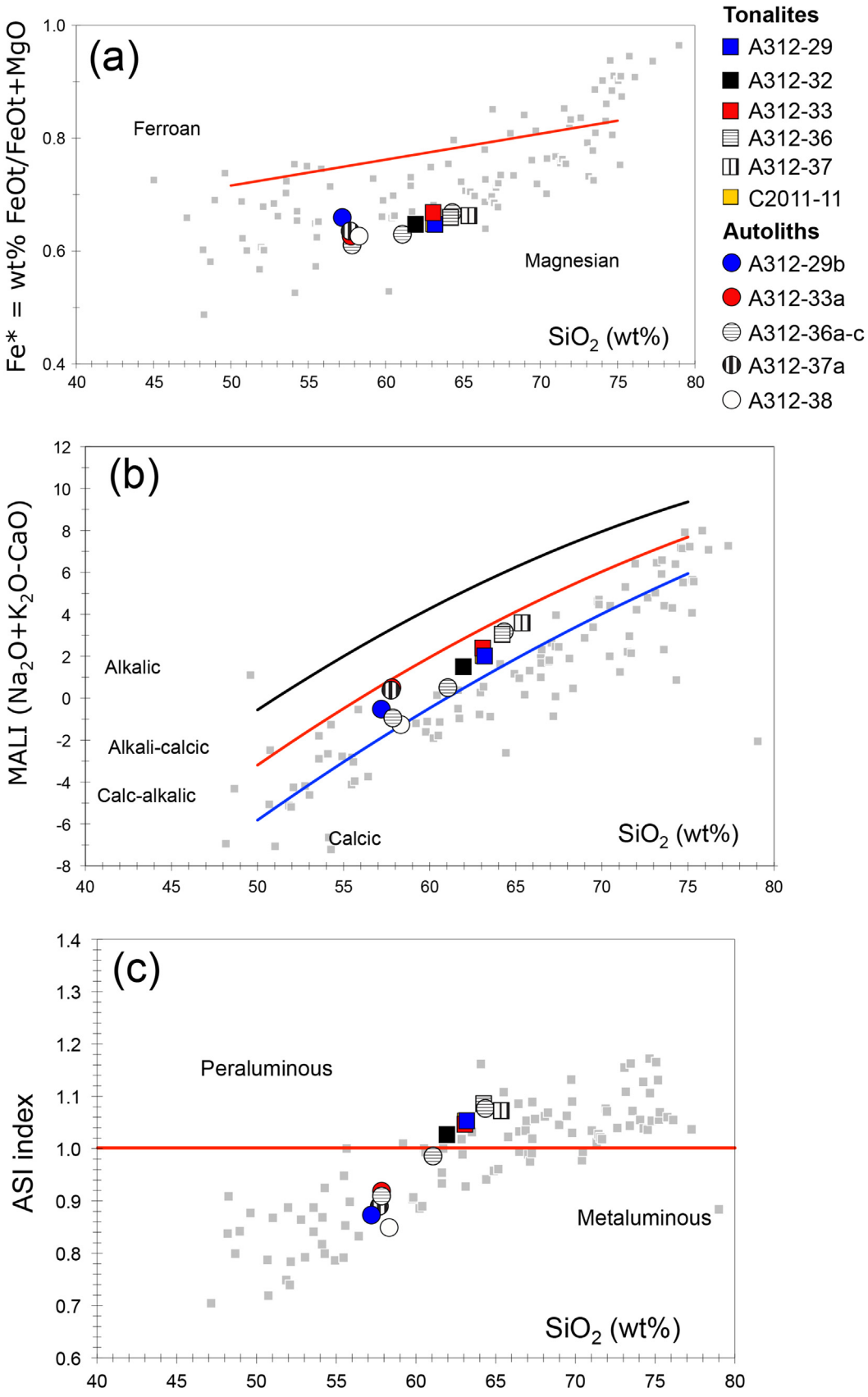

Fig. 4. Classification diagrams for Cerro Munro tonalites and autoliths. (a) Fe* vs SiO_2 diagram shows the magnesian character of both tonalites and autoliths. (b) MALI index indicates that Cerro Munro magmatic system have a calc-alkalic composition. (c) The ASI index separates the autoliths as metaluminous and the tonalites as peraluminous. Grey dots represent data from Patagonian Batholith (Argentina), taken as representative of calc-alkaline magmas.

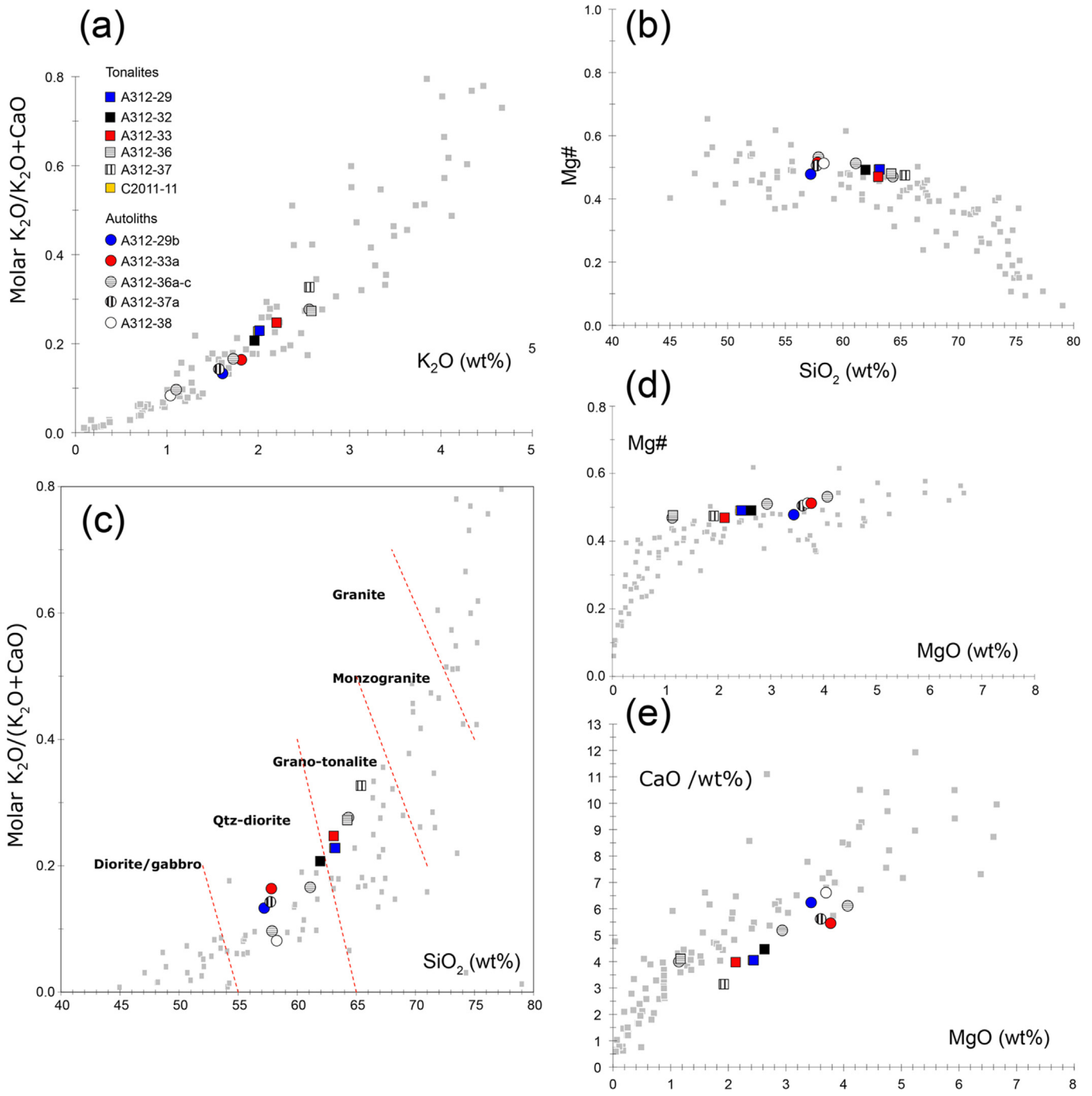

Fig. 5. Variation diagrams for Cerro Munro tonalites and autoliths. (a) Molar ratio K2O/K_2O + CaO vs K_2O diagram indicated the calc-alkaline trend by which tonalites and autoliths are differentiated. (b) Mg number maintains high values as the silica content (wt%) increases, away from the trend marked by the Patagonian batholith (grey dots). (c) Molar ratio K_2O/K_2O + CaO vs K_2O plot classifies the autoliths as Qz-diorite and host-rocks as grano-tonalites. The relation of Mg# (d) and CaO (e) with Mg denotes the decoupling of the Cerro Munro samples from the calc-alkaline trend.

be explained by FeO depletion for the Mg-poorer samples. This impoverishment is accompanied by a further depletion in CaO (wt %), separating the Cerro Munro differentiation path from the cotectic line marked by the Patagonian Batholith (Fig. 5e). Cpx and Fe-oxides fractionation can explain this detachment from the calc-alkaline cotectic line, due to a FeO and CaO impoverishment. More-depleted ends correspond to tonalites whereas autoliths show a scattered pattern (Figs. 4 and 5).

REE diagrams (Fig. 6) show slight differences between autoliths and the host tonalites, except for the case of the tonalite A312-36 (Fig. 6c), whose autoliths evidence a wide range of compositional variation between themselves and regarding the host tonalite. Autoliths A312-36b and c are the more primitive ends whereas the autolith 36a and the tonalite A312-36 are the more evolved ends, showing an amphibole or clinopyroxene fractionation pattern. For samples A312-33 and 33a the correlation is similar, the autolith

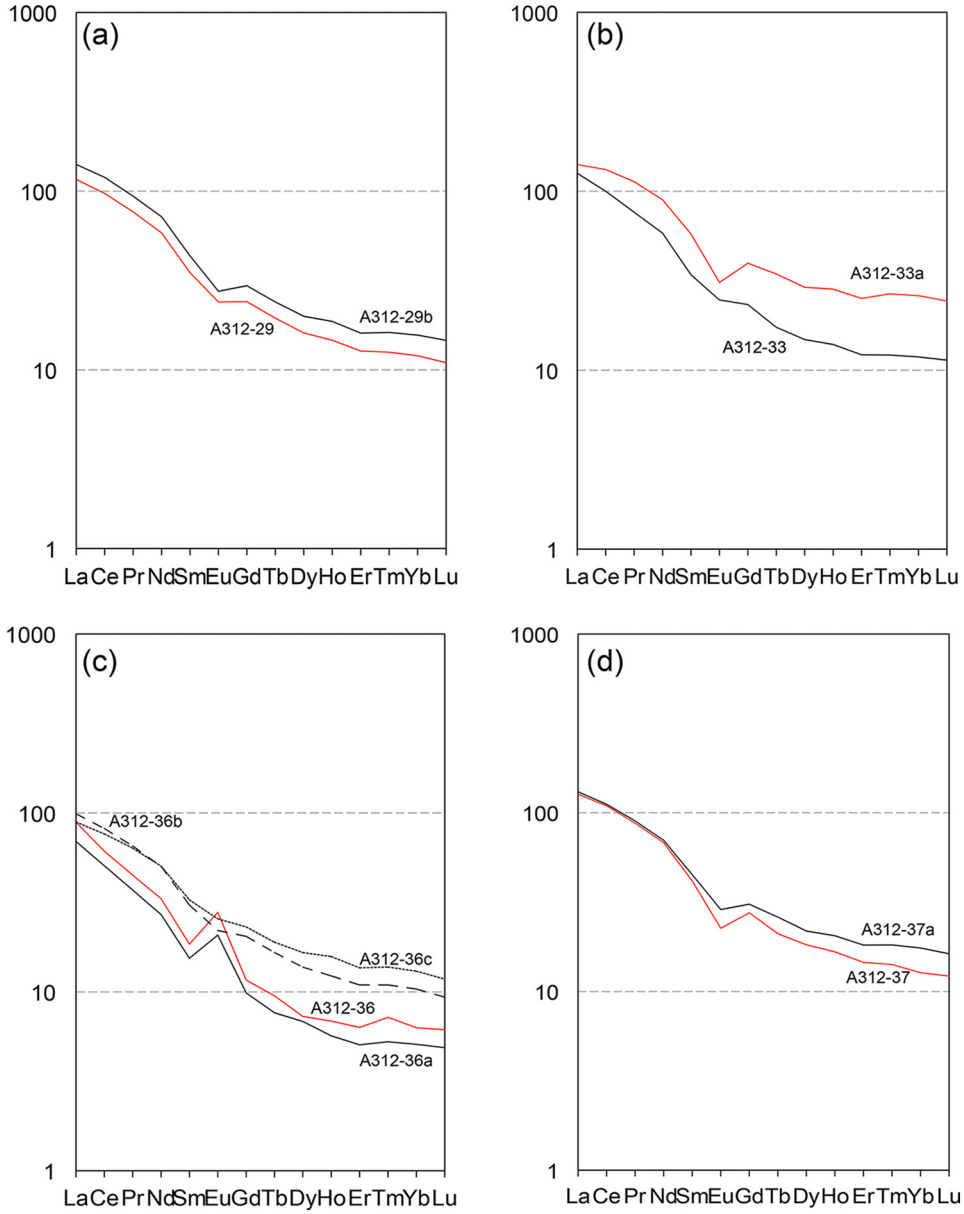

Fig. 6. REE spider diagrams, normalized to primitive mantle (Sun and McDonough, 1989), showing the relation of the tonalites (red curves) with their respective autoliths (black curves). (For interpretation of the references to colour in this figure legend, the reader is referred to the web version of this article.)

becoming richer in heavy REE and the tonalite following an Amp or Cpx fractionation pattern (Fig. 6b). These REE pattern support a double fractionation process resulting in autolith and tonalites from Cerro Munro intrusion.

6. Petrography of the Cerro Munro tonalite and related autoliths

6.1. Tonalites

These are medium-grained, mesocratic and homogeneous rocks composed of Pl, Amp, Kfs, Qz, Opaques, Bt, ± Cpx as essential minerals. Accessory minerals are Ap, Zrn, Allanite and Sphene (Fig. 7).

Plagioclase appears as euhedral to subhedral crystals, complexly zoned with patches and oscillatory bands (Fig. 7a), ranging in composition from An 0.5 at the cores to An 0.18 near the rims (Table 2 and Fig. 8a). Plagioclase cores show patching zoning and are surrounded by finely oscillatory layers in which resorption surfaces may be present (Fig. 7a). Patching zoning cores may content tiny inclusions of pyroxene (Fig. 7a). Plagioclase crystals form an interlocked framework and cumulate textures (Fig. 7b) in which quartz and occasionally K-feldspar occupy the interstices giving rise to graphic texture.

Amphiboles tend to form euhedral crystals, partially moulded by plagioclase (Fig. 7c). Note that amphibole is not present as inclusion in tonalites, showing features of an early phase precipitated from a water-rich magma (Fig. 7d). They range in composition from Mg-hornblende to actinolite (Table 3 and Fig. 8b) and contain inclusions of Ilm and Ti-Mt (Table S1). Actinolite occurs often at the rims of amphibole crystals in autoliths (Table 6 and Fig. 8b). Amphibole also may appear forming polycrystalline aggregates

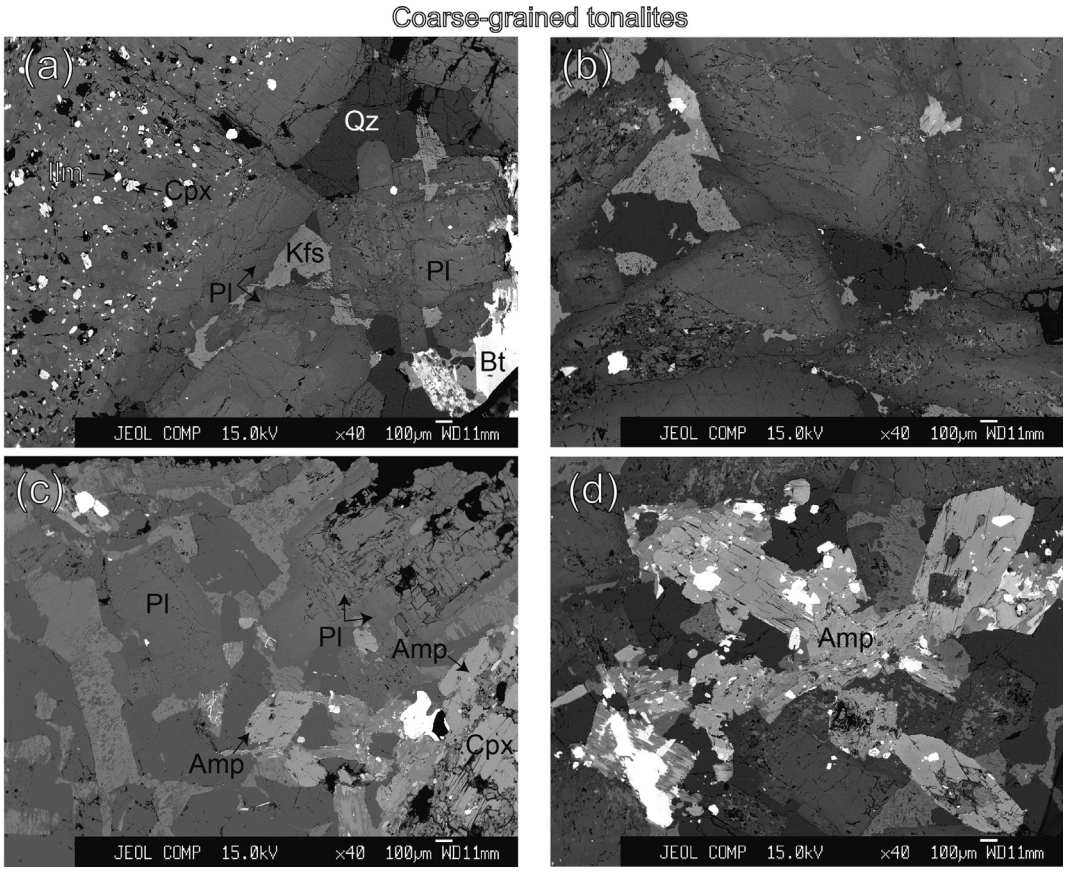

Fig. 7. BSE images of tonalites from Cerro Munro body. (a) Plagioclase phenocrysts have zoning and inclusions of Fe-Ti oxides and Clinopyroxene. Plagioclase is arranged forming cumulate texture and interstices filled by Qz and Kfs (b). Amphibole is present as phenocryst and replacing Cpx rim (c). Amphibole clots also occur (d). Mineral abbreviations after Whitney and Evans (2010).

(Fig. 7d).

Clinopyroxene (Mg# = 0.75; Table 4 and Fig. 8c) is partially transformed to amphibole and it occurs as both inclusion and relict cores (Fig. 7a and c).

Biotite (Mg# = 0.66, Table S2) appears as subhedral and anhedral crystals, in some cases, partially chloritized, and with inclusions of apatite, zircon and opaques (Fig. 7a and d). Fluorapatite, with up to 4.8 wt% of F, shows euhedral habit and also is included in Amp and Pl crystals. Garnet (grossular) is present as an accessory mineral in some samples of tonalites.

6.2. Autoliths

These are fine-grained rocks formed by the same similar assemblages than the host tonalite, except for the presence of Opx and the greater abundance of Cpx. Subtle differences in textures and modal abundances are found in comparison with the tonalite. Plagioclase shows habit euhedral (Fig. 9) and zoning, ranging the composition from An 0.67 at the core to An 0.16 (Table 5, Fig. 8a). Amphibole (from Mg-Fe-hornblende to actinolite; Table 6, Fig. 8b) tends to form acicular phenocrysts (Fig. 9a) and, together with magnetite (Ti-Mt; Table S1), are slightly more abundant with respect to the host tonalite. The early crystallization of amphibole can be evidenced by their preferential growth regarding the plagioclase (Fig. 9a). Amphibole polycrystalline aggregates may be present (Fig. 9b). Plagioclase and amphibole result in polycrystalline frameworks, leaving the interstices occupied by Kfs and Qz (Fig. 9c and d). Fluorapatite has an acicular habit (Fig. 9c). Clinopyroxene (Table 7, Fig. 8c) is present as inclusion in Pl, as relict core in Amp and forming subhedral crystals with oxide inclusions (Fig. 9d). Orthopyroxene (Table 7) appears as relict core in amphibole crystals and as inclusion in Pl. Autoliths mineralogy suggests a greater pressure for the magmatic source, at which the clinopyroxene and orthopyroxene can be stable.

Garnet (grossular) is only present in the autolith A312-36a, being the autolith more similar to tonalites regarding its geochemistry and petrography.

7. U-Pb SHRIMP zircon geochronology: sample description and results

7.1. Methodology

One sample of the intrusive rocks was selected with caution to avoid the marginal zones of the pluton and was analysed for zircon geochronology. Sample C.2011-11 from the Cerro Munro tonalite (Location 43° 12.86′S 70° 16.64′W; Fig. 2) is a fine-grained biotite-hornblende granodiorite. The texture is subidiomorphic and the modal mineralogy includes zoned plagioclase, hornblende, biotite and interstitial quartz and K-feldspar, with some cases of perthitic

Table 2
Microprobe analyses of plagioclases from the Cerro Munro tonalites.

Sample	29	29	29	29	29	29	32	32	32	33	33	33	33	33	36	36	36	36	36	36	37	37	37	37	37	37
Run	29–4	29–5	29–6	29–7	29 −12	29 −13	29 −14	29 −15	32–4	32–7	32 −11	32 −12	32 −13	33–2	33–3	33–4	33–5	33–6	33–7	36–1	36 −17	36 −18	36 −24	36 −25	36 −27	37–5	37 −17	37 −18	37 −19	37 −26	37 −27
Position[a]	inc	core	int	rim	core	int	int	rim	core	rim	core	int	rim	core	int	int	int	int	rim	int	rim	rim	core	int	rim	int	rim	int	core	rim	rim	core
SiO_2	65.81	58.94	57.59	63.83	59.31	56.71	60.49	62.96	58.67	65.51	61.14	56.44	60.34	56.22	59.49	59.11	58.15	58.94	58.47	59.35	58.93	64.57	60.65	55.33	62.78	62.49	63.39	54.93	56.41	64.11	55.57
Al_2O_3	21.61	25.87	26.79	22.39	25.66	27.55	25.02	23.40	25.79	21.56	23.79	26.98	24.22	27.60	25.30	25.71	26.43	25.67	25.99	25.59	25.64	22.21	24.75	28.08	22.85	23.24	22.74	28.61	27.29	21.96	27.16
FeO	0.31	0.26	0.21	0.14	0.38	0.28	0.31	0.25	0.35	0.12	0.34	0.41	0.32	0.35	0.28	0.37	0.33	0.30	0.27	0.32	0.24		0.30	0.29	0.20	0.21	0.30	0.32	0.30	0.19	0.36
CaO	2.36	7.20	8.28	3.09	7.06	9.08	6.31	4.38	7.47	2.27	5.17	8.71	5.48	9.33	6.77	7.13	7.91	7.17	7.50	6.46	6.75	2.11	5.55	9.44	3.35	4.34	3.86	10.42	9.11	2.52	9.23
Na_2O	9.77	7.15	6.71	9.33	7.36	6.08	7.47	8.72	7.02	9.87	8.37	6.69	8.26	5.89	7.22	6.93	6.60	6.86	6.67	7.48	7.13	9.53	7.60	5.61	9.59	8.85	9.23	5.53	6.18	9.84	6.05
K_2O	0.62	0.45	0.31	0.78	0.54	0.32	0.58	0.59	0.43	0.71	0.87	0.38	0.48	0.36	0.60	0.52	0.44	0.50	0.40	0.45	0.33	0.14	0.61	0.29	0.43	0.67	0.47	0.25	0.35	0.72	0.28
BaO	0.01		0.08	0.04	0.02	0.03	0.06	0.22		0.06	0.06	0.09	0.08	0.04	0.06	0.06	0.01	0.05	0.06	0.07	0.07	0.04		0.12	0.09	0.06	0.09	0.12	0.06	0.13	0.03
Total	100.6	99.97	100.2	99.67	100.5	100.2	100.4	100.8	99.95	100.2	100.0	99.88	99.36	99.98	99.89	100.1	100.1	99.73	99.52	100.0	99.34	98.74	99.82	99.49	99.43	100.0	100.2	100.3	99.88	99.65	98.83
X_{An}	0.11	0.35	0.40	0.15	0.34	0.44	0.31	0.21	0.36	0.11	0.24	0.41	0.26	0.46	0.33	0.35	0.39	0.36	0.37	0.31	0.34	0.11	0.28	0.47	0.16	0.21	0.18	0.50	0.44	0.12	0.45
X_{Ab}	0.85	0.63	0.58	0.81	0.63	0.54	0.66	0.76	0.61	0.85	0.71	0.57	0.71	0.52	0.64	0.62	0.59	0.62	0.60	0.66	0.64	0.88	0.69	0.51	0.82	0.76	0.79	0.48	0.54	0.84	0.53
X_{Or}	0.04	0.03	0.02	0.04	0.03	0.02	0.03	0.03	0.02	0.04	0.05	0.02	0.03	0.02	0.03	0.03	0.03	0.03	0.02	0.03	0.02	0.01	0.04	0.04	0.02	0.04	0.03	0.01	0.02	0.04	0.02

inc: phase included in Amp.
[a] Position represent the relative position of spot analyses within the crystal: int — intermediate between core and border.

and graphic textures. The rock has abundant inclusions of fine-grained mafic rich enclaves. Apatite, titanite, zircon and opaque minerals are present as accessory minerals.

The sample (C.2011-11) selected for the geochronological study, was crushed and milled to a medium and fine grain fraction at the National University of La Plata (Argentina). Zircon separation was accomplished at the University of Huelva by traditional techniques using dense liquids and magnetic separation (Frantz). Selected crystals free of impurities and fractures were selected by hand-picking with a binocular lens.

Analyses were carried out in the SHRIMP II microprobe at Beijing SHRIMP Center. Analytical procedures are as follows. Zircon grains were mounted in epoxy, together with reference standards SL13 (U = 238) and TEMORA ($^{206}Pb/^{238}U = 0.06683$), and polished. Sectioned zircons were studied by CL imaging for selection of point analyses. The mounts were then cleaned and coated with high-purity Au. Core and rims were analysed in several grains of each individual sample with the aim of identifying inherited cores. These selected points were target over the CL images and analysed for U-Th-Pb isotopes with SHRIMP II at the Beijing-SHRIMP Center (Chinese Academy of Geological Sciences, Beijing), following methods given in (Williams, 1998) and references therein. A 10 kV negative O_2 primary beam was focused to c. 20 mm diameter. Positive secondary ions were extracted at 10 kV and mass analysed at c. R5000 on a single ETP multiplier by peak stepping through the isotopes of interest. Analytical uncertainties are 1s precision estimates. All the analyses listed and plotted were corrected for common Pb using the measured ^{204}Pb and a common Pb composition appropriate to the age of each spot (Cumming and Richards, 1975). Concordia ages have been calculated with ISOPLOT 3.0 software (Ludwig, 2003). Uncertainties are 95% confidence limits ($t\sigma$, where t is the student's t multiplier) and include the uncertainty in the Pb/U calibration (ca. 0.3–0.5%). Ages were calculated with λ errors and MSWD was determined using Concord. + Equiv. Ages were calculated using the constants recommended by the IUGS Subcommission on Geochronology (Steiger and Jäger, 1977).

7.2. U-Th-Pb geochronology results

The sample from Cerro Munro (C.2011-11) intrusive body was analysed for U-Th-Pb in the SHRIMP II microprobe at Beijing SHRIMP Center. Zircon populations (Fig. 10) are euhedral to subhedral medium-large crystals (120–300 μm). CL images show simple internal structures in zircons, with parallel-banded zoning in more elongated crystals and concentric or absent zoning in less acicular zircons (Fig. 10a). Th/U ratios are comprised between 0.6 and 1.56, mostly higher in C.2011-11 sample, showing no relation with U-Pb ages. Location of sample is given in Fig. 2. Analytical results are listed in Table 8. Analysed zircon crystals and spots from each sample are shown in Fig. 10 together with concordia diagrams. We can distinguish between acicular crystals, with parallel-banded zoning, and flattened zircons with a very weak or absent zoning pattern (Fig. 10). Ten analyses with $^{206}Pb/^{238}U$ ages between 59.6 ± 2.7 and 53.8 ± 2.1 Ma, yield a concordia age of 57.1 ± 1.4 Ma (MSWD = 0.7).

8. Cathodoluminiscence and EBSD study in volcanic quartz

In order to know the volcanic process generating rhyolite dikes hosted in Cerro Munro tonalite, textural analysis was performed in Qz phenocrysts from a rhyolitic porphyry. This porphyry cut Cerro Munro intrusion but not the country rocks (sample 34 in Fig. 2).

Cathodoluminiscence studies in Qz from a rhyolite porphyry was carried out by an Environmental Scanning Electron Microscopy (ESEM, FEI Quanta 400) coupled with a cathodoluminiscence

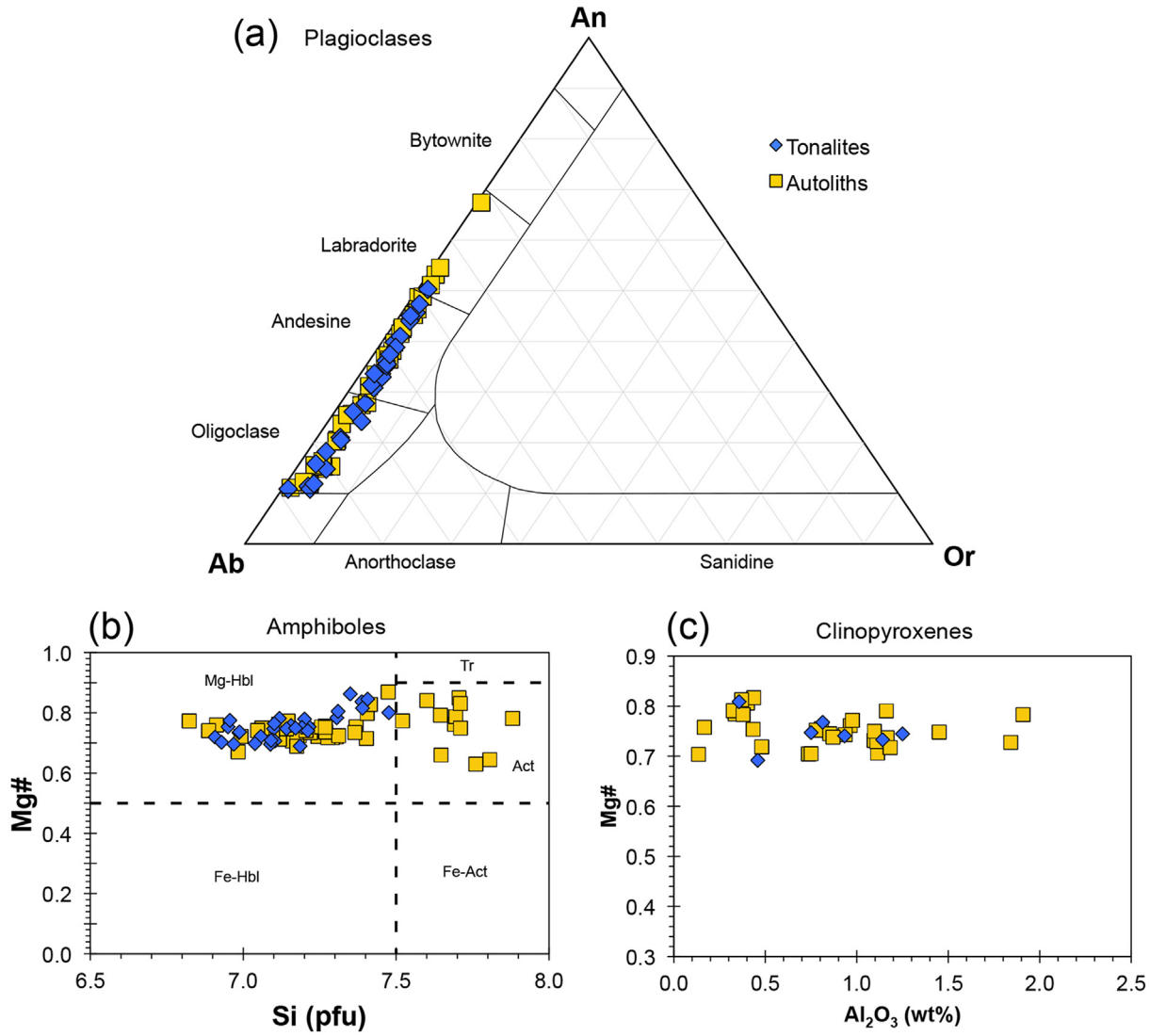

Fig. 8. Classification diagrams for plagioclase according to anorthite (X_{An}) and albite (X_{Ab}) molar fraction (a), for calcic amphiboles (b) and clinopyroxenes (c). Amphibole classification after Leake et al. (1997). Tonalites are represented by blue diamonds and autoliths by yellow squares. Si cation proportion is represented per formula unit. (For interpretation of the references to colour in this figure legend, the reader is referred to the web version of this article.)

detector (ChromaCL, Gatan), at the CIC, University of Granada (Spain). The Electron back-scattered diffraction (EBSD) was conducted by a High-Resolution Scanning Electron Microscopy (HRSEM, AURIGA (FIB-FESEM) from Carl Zeiss SMT), also at the CIC, University of Granada (Spain). The sample was polished with colloidal silica of 0.01 μm of grain size for the cathodoluminiscence and EBSD study.

Quartz crystals were selected from the rhyolitic porphyry (sample A312-34; Table 1) for the cathodoluminiscence and electron back-scattered diffraction study (Fig. 11). The Qz core is zoned showing a previous crystalline orientation within a spherical crystal, giving rise to a circular shape of this previous crystal (Fig. 11b). Circular shapes of magmatic crystals have been described in relation to melt-rich environments (Kirkpatrick, 1981). Subsequently, Qz crystallization progresses following the same crystal orientation (Fig. 11d) and according to well-developed crystal faces. This development of euhedral shapes is related to fluid-rich regions where the ion mobility is high (Sunagawa, 1981). The myrmekite rims around the main crystal (Fig. 11b), which also follow the orientation along the c axis (Fig. 11d), evidence a final episode of Qz growth. The cathodoluminiscence image of Qz (Fig. 11) sheds light about the batch-fractionation processes occurring in the magma chamber of the Cerro Munro body, in two stages at least (double fractionation). During an early crystallization stage, the quartz crystallizes in a melt-rich magma. However, during the late solidification stage, the quartz is able to crystallize developing a euhedral shape, in equilibrium with fluid-rich environments. Although the real colour of CL images is not considered a reliable tool to identify the Qz origin, the blue colour in CL images of Qz (Fig. 11b) is usually related to the volcanic origin (Boggs et al., 2002). Also, this blue luminescence has been associated to high Al contents (Ramseyer and Mullis, 1990). However the red colour occurring in the myrmekite rim (Fig. 11b) is linked to volcanic sills and dikes (Ramseyer et al., 1988; Ramseyer and Mullis, 2000).

9. Discussion

Processes related to the cooling history of magma chambers are inferred through the petrographic, geochemical and geochronological study of plutons and volcanic rocks (Bachmann and

Table 3
Microprobe analyses of amphiboles from the Cerro Munro tonalites.

Sample	29	29	29	29	29	32	32	32	32	32	32	36	36	36	36	36	36	36
Run	291	293	298	2911	2917	321	329	3210	3217	3222	3223	362	367	368	369	3612	3613	3621
Position[a]	int	int	core	core	core	int	core	rim	core	core	int	core	rim	core	int	core	rim	int
SiO_2	49.30	49.60	49.07	50.35	49.81	50.19	48.97	52.36	47.79	47.56	51.78	47.12	52.32	49.28	49.29	47.54	51.90	49.22
TiO_2	1.51	1.31	1.38	1.11	1.29	1.24	1.36	0.68	1.66	1.87	0.71	1.67	0.80	1.08	1.06	1.57	0.72	1.35
Al_2O_3	5.59	5.29	5.74	4.57	5.01	4.74	5.13	3.42	6.52	6.62	3.48	6.19	3.27	4.57	4.38	5.95	3.54	4.94
Cr_2O_3		0.00		0.06	0.08	0.09	0.03	0.09	0.02	0.07		0.03	0.06			0.03	0.04	
FeO	11.73	11.48	10.97	12.91	12.55	11.49	12.62	9.86	11.37	12.58	9.84	12.31	9.04	12.72	13.45	11.95	8.91	12.42
MnO	0.20	0.20	0.23	0.27	0.30	0.26	0.32	0.11	0.16	0.29	0.14	0.19	0.21	0.31	0.34	0.21	0.09	0.29
MgO	16.21	16.59	16.43	15.98	15.97	16.60	15.45	18.49	16.07	15.28	18.01	15.80	18.73	15.75	15.39	15.94	19.00	15.58
NiO	0.04	0.05	0.03	0.12	0.02	0.02	0.04	0.09		0.06	0.10	0.03	0.04	0.05		0.01	0.05	0.06
CaO	11.31	11.22	11.15	11.05	11.06	11.12	10.83	11.43	10.94	11.00	11.68	11.00	11.78	11.10	11.04	11.07	11.69	11.18
Na_2O	1.63	1.54	1.65	1.40	1.43	1.58	1.51	1.25	2.02	2.03	1.31	1.59	1.01	1.31	1.12	1.58	1.06	1.22
K_2O	0.51	0.49	0.52	0.41	0.50	0.45	0.48	0.38	0.60	0.64	0.38	0.57	0.34	0.43	0.43	0.52	0.40	0.45
F	0.09	0.36	0.31	0.27	0.23	0.57	0.69	1.15	0.73	1.32	1.20	0.75	0.61	0.78	0.83	0.45	1.01	0.69
Total	98.10	98.13	97.48	98.5	98.24	98.34	97.42	99.29	97.87	99.33	98.63	97.25	98.20	97.38	97.30	96.82	98.41	97.4
Si (T)[b]	7.10	7.12	7.10	7.22	7.16	7.20	7.14	7.39	6.95	6.91	7.39	6.97	7.41	7.19	7.21	6.96	7.35	7.17
Al (T)	0.90	0.88	0.90	0.77	0.84	0.80	0.86	0.57	1.05	1.09	0.59	1.03	0.55	0.79	0.75	1.03	0.59	0.83
Ti (T)				0.01				0.04			0.02		0.05	0.02	0.03	0.02	0.06	
Ti (C)	0.16	0.14	0.15	0.11	0.14	0.13	0.15	0.03	0.18	0.20	0.05	0.19	0.04	0.10	0.08	0.15	0.02	0.15
Al (C)	0.05	0.01	0.08		0.01	0.00	0.02		0.07	0.04		0.05						0.02
Cr (C)				0.01	0.01	0.01	0.00	0.01	0.00	0.01		0.00	0.01			0.00	0.01	
Fe^{3+} (C)	0.23	0.39	0.23	0.44	0.42	0.37	0.40	0.40	0.24	0.24	0.30		0.35	0.42	0.48	0.45	0.42	0.38
Ni (C)	0.00	0.01	0.00	0.01	0.00	0.00	0.00	0.01		0.01	0.01	0.00	0.01	0.01		0.00	0.01	0.01
Fe^{2+} (C)	1.08	0.90	0.99	1.02	1.01	0.93	1.06	0.66	1.02	1.19	0.80	1.27	0.65	1.05	1.09	0.91	0.54	1.06
Mg (C)	3.48	3.55	3.54	3.42	3.42	3.55	3.36	3.89	3.48	3.31	3.83	3.48	3.95	3.43	3.36	3.48	4.01	3.39
Mn^{2+} (B)	0.02	0.02	0.03	0.03	0.04	0.03	0.04	0.01	0.02	0.04	0.02	0.02	0.03	0.04	0.04	0.03	0.01	0.04
Fe^{2+} (B)	0.11	0.09	0.11	0.09	0.08	0.08	0.08	0.10	0.12	0.10	0.07	0.25	0.08	0.08	0.08	0.10	0.10	0.07
Ca (B)	1.75	1.73	1.73	1.70	1.70	1.71	1.69	1.73	1.71	1.71	1.79	1.73	1.79	1.74	1.73	1.74	1.77	1.75
Na (B)	0.12	0.16	0.14	0.18	0.18	0.19	0.19	0.16	0.16	0.15	0.13		0.11	0.14	0.14	0.14	0.12	0.15
Na (A)	0.33	0.27	0.33	0.21	0.22	0.26	0.23	0.19	0.41	0.42	0.23	0.46	0.16	0.23	0.18	0.31	0.17	0.20
K (A)	0.09	0.09	0.10	0.08	0.09	0.08	0.09	0.07	0.11	0.12	0.07	0.11	0.06	0.08	0.08	0.10	0.07	0.08
OH (W)	1.96	1.84	1.86	1.88	1.90	1.74	1.68	1.49	1.67	1.39	1.46	1.65	1.73	1.64	1.62	1.79	1.55	1.68
F (W)	0.04	0.16	0.14	0.12	0.10	0.26	0.32	0.51	0.34	0.61	0.54	0.35	0.28	0.36	0.38	0.21	0.45	0.32
Cl (W)	n.a.	n.a.	n.a.	n.a.	n.a.	n.a.	n.a.	n.a.	n.a.	n.a.	n.a.	n.a.	n.a.	n.a.	n.a.	n.a.	n.a.	n.a.
Sum T,C,B,A	15.42	15.36	15.42	15.29	15.31	15.34	15.32	15.25	15.52	15.54	15.31	15.58	15.23	15.31	15.26	15.40	15.25	15.28
#Mg	0.75	0.78	0.76	0.75	0.76	0.78	0.75	0.84	0.75	0.72	0.81	0.70	0.85	0.75	0.74	0.77	0.86	0.75
P (kbar)[c]	0.64	0.69	0.77	0.58	0.64	0.60	0.68	0.44	0.94	0.96	0.44	0.88	0.42	0.59	0.56	0.83	0.45	0.64

Sample	37	37	37	37	37	37	37	37	37	37	37	37	37
Run	371	374	378	379	3710	3711	3715	3716	3721	3722	3725	3729	3731
Position[a]	int	int	core	int	rim	core	rim	int	core	rim	rim	int	int
SiO_2	48.55	48.64	50.81	47.40	52.27	48.89	48.36	47.99	48.16	50.92	49.30	48.89	48.09
TiO_2	1.36	1.54	1.08	1.55	0.61	1.50	1.53	1.72	1.39	0.79	1.18	1.54	1.65
Al_2O_3	5.30	5.57	3.80	6.33	3.01	5.33	5.64	6.03	5.19	3.98	4.71	5.55	5.88
Cr_2O_3				0.11	0.03		0.15	0.00		0.07			0.04
FeO	13.35	12.82	11.63	13.57	10.35	13.56	13.91	12.27	13.85	9.43	14.35	13.32	12.35
MnO	0.29	0.21	0.27	0.26	0.31	0.29	0.34	0.30	0.31	0.24	0.37	0.30	0.24
MgO	15.27	15.63	16.86	14.97	17.63	15.19	14.90	15.70	14.89	18.09	14.94	15.23	15.85
NiO	0.04	0.01	0.01	0.03		0.07	0.06				0.00	0.00	0.08
CaO	10.87	10.93	11.07	10.89	11.55	10.73	10.79	10.84	10.83	11.56	10.76	10.82	10.98
Na_2O	1.78	1.96	1.40	2.05	1.20	1.81	1.79	2.02	1.82	1.59	1.74	1.78	2.00
K_2O	0.51	0.54	0.40	0.59	0.30	0.50	0.53	0.54	0.50	0.52	0.49	0.51	0.50
F	1.33	1.20	1.53	1.30	1.14	1.54	1.26	0.81	1.26	2.03	1.19	1.21	0.76
Total	98.62	99.06	98.86	99.04	98.39	99.41	99.25	98.21	98.19	99.22	99.03	99.14	98.4
Si (T)[b]	7.10	7.06	7.31	6.93	7.48	7.10	7.04	6.99	7.09	7.31	7.19	7.09	6.99
Al (T)	0.90	0.94	0.64	1.07	0.51	0.90	0.96	1.01	0.90	0.67	0.81	0.91	1.01
Ti (T)			0.05		0.02				0.01	0.01	0.01		0.00
Ti (C)	0.15	0.17	0.07	0.17	0.05	0.16	0.17	0.19	0.15	0.07	0.12	0.17	0.18
Al (C)	0.01	0.01		0.02		0.02	0.01	0.02				0.04	
Cr (C)				0.01	0.00		0.02			0.01			0.00
Fe^{3+} (C)	0.28	0.25	0.40	0.28	0.30	0.28	0.29	0.26	0.27	0.20	0.29	0.27	0.27
Ni (C)	0.00	0.00	0.00	0.00		0.01	0.01						0.01
Fe^{2+} (C)	1.24	1.19	0.92	1.26	0.89	1.24	1.28	1.12	1.32	0.85	1.34	1.23	1.11
Mg (C)	3.33	3.38	3.61	3.26	3.76	3.29	3.23	3.41	3.27	3.87	3.25	3.29	3.43
Mn^{2+} (B)	0.04	0.03	0.03	0.03	0.04	0.04	0.04	0.04	0.04	0.03	0.05	0.04	0.03
Fe^{2+} (B)	0.12	0.12	0.08	0.13	0.05	0.13	0.13	0.11	0.12	0.08	0.12	0.12	0.13
Ca (B)	1.70	1.70	1.71	1.71	1.77	1.67	1.68	1.69	1.71	1.78	1.68	1.68	1.71
Na (B)	0.14	0.15	0.18	0.14	0.14	0.17	0.15	0.16	0.14	0.11	0.15	0.16	0.14
Na (A)	0.36	0.40	0.21	0.45	0.19	0.34	0.36	0.41	0.38	0.34	0.34	0.34	0.43
K (A)	0.09	0.10	0.07	0.11	0.06	0.09	0.10	0.10	0.09	0.10	0.09	0.09	0.09
OH (W)	1.38	1.45	1.30	1.40	1.48	1.29	1.42	1.63	1.42	1.08	1.45	1.44	1.65

Table 3 (*continued*)

Sample	37	37	37	37	37	37	37	37	37	37	37	37	37
Run	371	374	378	379	3710	3711	3715	3716	3721	3722	3725	3729	3731
Position[a]	int	int	core	int	rim	core	rim	int	core	rim	rim	int	int
F (W)	0.62	0.55	0.70	0.60	0.52	0.71	0.58	0.37	0.58	0.92	0.55	0.56	0.35
Cl (W)	n.a.	n.a.	n.a.	n.a.	n.a.	n.a.	n.a.	n.a.	n.a.	n.a.	n.a.	n.a.	n.a.
Sum T,C,B,A	15.46	15.50	15.29	15.55	15.24	15.43	15.46	15.51	15.47	15.43	15.43	15.43	15.52
#Mg	0.71	0.72	0.78	0.70	0.80	0.71	0.70	0.73	0.69	0.81	0.69	0.71	0.74
P (kbar)[c]	0.70	0.75	0.49	0.90	0.40	0.70	0.76	0.84	0.69	0.50	0.61	0.74	0.80

[a] Position represent the relative position of spot analyses within the crystal: int — intermediate between core and border.
[b] Structural amphibole formula was calculated according to Locock (2014).
[c] Pressure obtained by Amp barometry from Ridolfi et al. (2010).

Table 4
Microprobe analyses of pyroxenes of the Cerro Munro tonalites.

Phase	Cpx	Cpx	Cpx	Cpx	Cpx	Cpx	Cpx
Sample	32 (relict core)	33 (inc)	33 (inc)	33 (inc)	36 (relict core)	36 (relict core)	37 (relict core)
Run	32–21	33–8	33–9	33–11	36–20	36–33	37–13
SiO_2	52.29	51.96	52.61	52.60	53.85	52.64	52.99
TiO_2	0.27	0.32	0.20	0.27	0.02	0.11	0.17
Al_2O_3	0.75	1.25	0.93	1.14	0.36	0.46	0.81
Cr_2O_3	0.06	0.09	0.05	n.d.	0.15	n.d.	0.03
FeO	8.79	8.91	8.98	9.42	6.45	10.62	8.22
MnO	0.39	0.33	0.34	0.35	0.32	0.33	0.51
MgO	14.62	14.60	14.37	14.48	15.32	13.33	15.21
NiO	0.00	n.d.	n.d.	0.02	n.d.	n.d.	0.02
CaO	21.54	21.48	21.76	21.67	23.08	21.94	21.49
Na_2O	0.49	0.42	0.44	0.43	0.21	0.37	0.38
K_2O	0.01	n.d.	0.01	0.00	0.02	n.d.	0.00
F	n.d.	0.15	n.d.	n.d.	0.17	0.13	0.03
Total	99.27	99.59	99.82	100.43	99.95	99.96	99.88
#Mg[a]	0.75	0.74	0.74	0.73	0.81	0.69	0.77

inc: phase included in Pl.
n.d.: not determined.
[a] Mg# = molar MgO/[MgO + FeO].

Bergantz, 2004; Bellos et al., 2015; Deering and Bachmann, 2010; Lipman and Bachmann, 2015). The relation between autoliths and hosting plutons can provide useful information about processes generating silicic magmas. Petrographical and geochemical tools are essential to understand the mechanisms connecting autoliths and its plutonic host.

The Cerro Munro tonalite is a good example of calc-alkaline magmatism in which the relation between tonalites and autoliths and dykes can address the cooling history. Textures, mineralogical and geochemical signatures record the processes occurring in a common magma chamber, such as cooling, recharge, recycling, assimilation and/or fractionation.

The geochemical correlation between autolith-host pairs indicates a basicity increase of the enclaves regarding the host tonalites from Cerro Munro intrusion (Figs. 4 and 5). The set of tonalites and autoliths can be expected to follow the typical differentiation pattern of calc-alkaline series, where the autoliths correspond to residues and the tonalites to more differentiated magmas. However, the fractionation pattern from the Cerro Munro body is separated from a calc-alkaline evolution, characterized by a constant Mg number (Fig. 5d) and CaO depletion (Fig. 5e). Given that the MgO content evolves according the calc-alkaline trend (Fig. 5d), only the FeO impoverishment justifies the constant Mg number for more evolved terms (Fig. 4a). The fractionation of mineral phases as Cpx and Fe-oxides can induce this FeO and CaO depletion for the tonalites. Thus, the geochemical signatures of Cerro Munro tonalites suggest a fractionation from a magma, which generated a residue rich in Cpx fenocrystals with Fe-oxides inclusions. This Cpx rich in Fe-oxides inclusions, left behind during the fractionation process, has been partially recorded in the mineralogy of the autoliths (Fig. 9d). The fractionation of a metaluminous phase (amphibole and/or clinopyroxene), preferentially subtracting Ca, also explains why autoliths are metaluminous whereas tonalites have a peraluminous signature (Fig. 4c).

Non-cotectic relations from the CaO-MgO diagram indicate a Cpx and Fe oxides fractionation, increasing their basicity and moving away the trend from the cotectic CaO-MgO variation (Fig. 5e). The fractionation of Fe oxides, hosted as inclusions in Cpx (Fig. 9d), maintains a high Mg# as magnesium decreases (Fig. 5d). At the same time, the Cpx fractionation separates the geochemical trend of Cerro Munro samples from the cotectic line, since the Ca content of the magma is less than what is expected, due to the Cpx loss.

On the other hand, both tonalites and autoliths show cumulate textures (Figs. 7 and 9), which indicates the segregation of a potentially eruptible, residual liquid. We deduce that these rocks can be the result of a double fractionation or fractionation by batches of a hydrous magma, supported by the contribution of the successive fractionated pulses of magma.

Other textural features as oscillatory zoning in Pl of tonalites

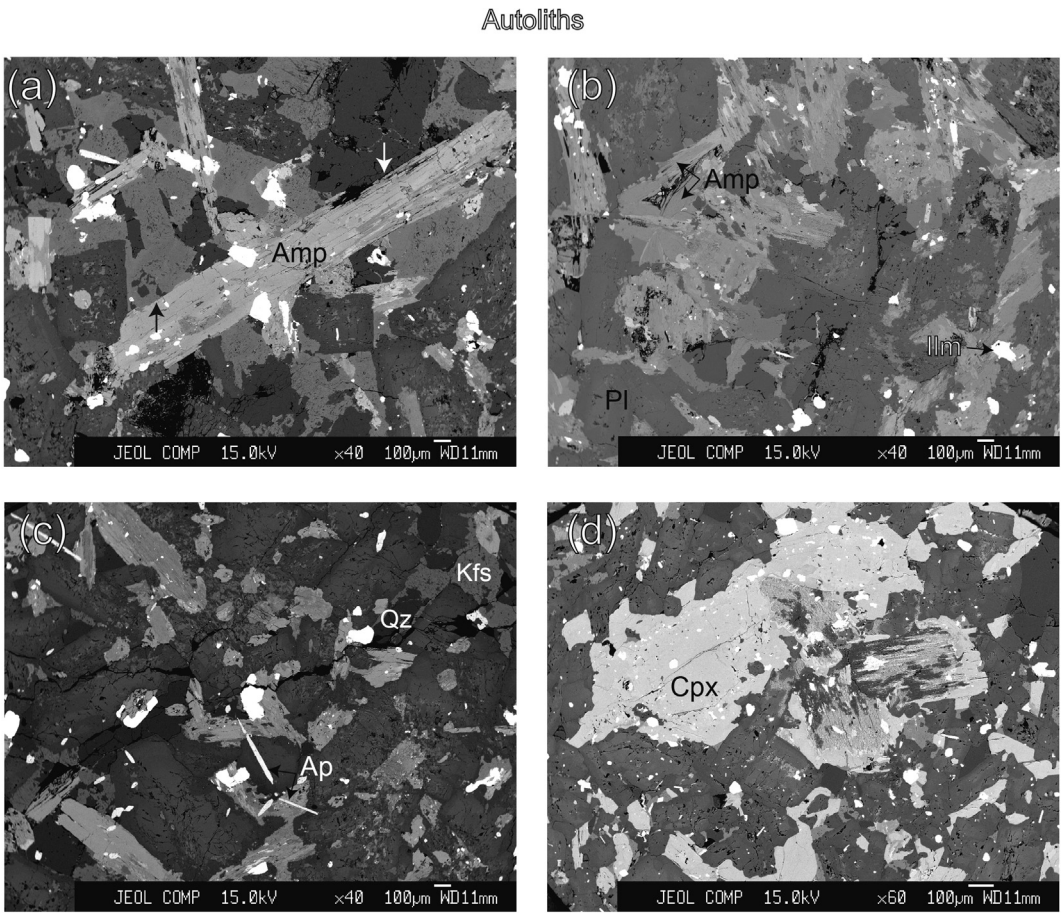

Fig. 9. BSE images of autoliths from Cerro Munro body. (a) Amphibole phenocryst indicates their early growth and high initial water contents. (b) Amp and Pl have smaller grain size in autoliths. (c) Acicular apatite also supports the high initial water contents of the magma. (d) Interstices are occupied by Qz and Kfs, forming graphic textures.

(Fig. 7a) and Qz from rhyolites (Fig. 11b) indicate different cooling episodes in the magmatic system. Na-rich rim in Pl (Table 2) and graphic textures at the interstices (Fig. 7b and c) in both tonalites and autoliths indicate final undercooling at near *solidus* stage. Also, textural features of autoliths, such as grain size, acicular apatite and amphibole, are indicative of undercooling. Pressure estimations in amphibole for both tonalites and autoliths constrain the depths of emplacement at shallow crustal levels corresponding to 0.6 kbar (Tables 3 and 6). The early growth of amphibole suggests a hydrous composition for the initial magma from which the autoliths crystallized.

Cumulate textures in both tonalites and autoliths (Figs. 7 and 9) suggest a liquid expulsion from a crystal mush. It is accompanied by the occurrence of amphibole phenocrysts and textures, indicating their presence as an early phase (Figs. 7d and 9a). This supports the theory that these rocks come from a water-rich magma. The amphibole saturation as *liquidus* phase is expected in wet magmas, at higher pressures and with high Na_2O contents (Fig. 4b and Table 1; Naney, 1983; Scaillet and Evans, 1999; Sisson and Grove, 1993). For this reason, it is not discarded that during the crystallization course, water saturation can be reached and pressure changes are considered during the magma ascent to the shallow level of emplacement.

Based on the features mentioned above, we can say that the enclaves may represent autoliths: fragments of early chilled margins of the intrusion dragged by mechanical erosion from the magma conduits or the walls of the early magma chamber. We cannot discard the provenance from a different, deeper magma chamber.

In spite of the cumulate textures in both tonalites and autoliths, few samples from Cerro Munro intrusion show REE enrichment patterns of cumulate rocks. Nonetheless, the Cpx or Amp fractionation pattern is found in both autoliths and tonalites (Fig. 6). The positive Eu anomaly (Fig. 6c; samples A312-36 and 36a) is only present in tonalite A312-36 and its enclave A312-36a, and coincides with high values for the Sr/Y ratio (Fig. 12) and the garnet occurrence. The Sr/Y ratio increases as Y decreases indicating an inherited pattern from the source-melting process involving garnet. The parental magma was fractionated at deeper levels, where the garnet was stable. From the HREE concave pattern of these samples -in which the differentiation is more evident-the amphibole and/or clinopyroxene role in the fractionation process can be deduced (Fig. 6c; A312-36 and 36a).

The study of cathodoluminiscence and electron back-scattered diffraction (EBSD) of Qz, from a rhyolite porphyry cutting the Cerro Munro tonalite, reveals this crystallization at different episodes, recording a first crystallization step disrupted by a later stage during which the fluid concentration is higher (Fig. 11b). This increase in the fluid content is explained by the segregation of the water-saturated melt, as a consequence of the second boiling (see further explanation). A final crystallization stage followed by a *subsolidus* solidification of Qz and Kfs is evidenced by CL images (Fig. 11b). Notes that the entire crystallization time frame of the Cerro Munro tonalite should coincide with the dating error range

Table 5
Microprobe analyses of plagioclases from the Cerro Munro autoliths.

Sample	29b	29b	29b	29b	29b	29b	29b	29b	29b	33a	33a	36A	36a	36a	36a	36a	36B	36B	36B	36B	36B	36B	36B
Run	29b-6	29b-7	29b-8	29b-9	29b-10	29b-19	29b-20	29b-25	29b-26	33a-12	33a-13	36A-2	36A-4	36A-8	36A-44	36A-46	36B-5	36B-6	36B-14	36B-15	36B-16	36B-17	36B-23
Position[a]	core	rim	core	int	rim	int	int	int	rim	core	rim	int	core	rim		inc	core	rim	core	rim	core	rim	inc
SiO_2	56.97	64.23	54.58	62.84	65.63	62.57	55.38	57.69	61.33	53.08	62.33	57.14	55.92	63.51	64.07	54.92	56.47	63.16	57.33	65.12	54.79	60.97	59.87
Al_2O_3	27.30	22.29	29.14	23.63	21.96	24.04	28.78	26.79	24.32	29.39	22.96	26.39	27.93	22.70	23.32	28.75	26.85	22.24	26.38	21.75	28.24	24.34	25.11
FeO	0.27	0.23	0.30	0.18	0.07	0.36	0.27	0.30	0.33	0.20	0.21	0.44	0.28	0.35	0.27	0.38	0.29	0.19	0.24	0.12	0.24	0.22	0.28
CaO	8.82	3.21	11.00	4.32	2.28	4.90	10.46	8.18	5.40	11.27	4.18	7.61	9.24	3.07	3.20	10.18	8.55	3.23	7.88	2.45	10.08	5.28	6.36
Na_2O	6.44	9.27	5.23	8.90	10.01	8.49	5.37	6.66	8.35	5.07	8.78	7.07	5.97	9.38	9.38	5.83	6.45	9.45	6.80	9.77	5.69	8.13	7.51
K_2O	0.28	0.85	0.19	0.55	0.18	0.38	0.24	0.31	0.47	0.19	0.55	0.39	0.32	0.56	0.66	0.15	0.31	0.40	0.40	0.61	0.24	0.46	0.42
BaO		0.09	0.02	0.05			0.12	0.06	0.16	0.04			0.05	0.06	0.02		0.08		0.05	0.06	0.07		0.03
Total	100.3	100.3	100.8	100.7	100.4	101.1	100.9	100.1	100.5	99.40	99.09	99.15	99.90	99.81	101.1	100.5	99.18	98.86	99.38	100.2	99.51	99.92	99.66
X_{An}	0.42	0.15	0.53	0.21	0.11	0.24	0.51	0.40	0.26	0.55	0.20	0.36	0.45	0.15	0.15	0.49	0.42	0.16	0.38	0.12	0.49	0.26	0.31
X_{Ab}	0.56	0.80	0.46	0.76	0.88	0.74	0.47	0.58	0.72	0.44	0.77	0.61	0.53	0.82	0.81	0.50	0.57	0.82	0.60	0.85	0.50	0.72	0.66
X_{Or}	0.02	0.05	0.01	0.03	0.01	0.02	0.01	0.02	0.03	0.01	0.03	0.02	0.02	0.03	0.04	0.01	0.02	0.02	0.02	0.03	0.01	0.03	0.02

Sample	37a	37a	37a	37a	37a	37a	38	38	38	38	38	38
Run	37a-3	37a-4	37a-5	37a-6	37a-13	37a-16	38–9	38–10	38–14	38–18	38–19	38–23
Position[a]	int	core	int	rim	int	core	core	rim	inc	core	rim	
SiO_2	57.90	54.80	58.20	64.38	59.06	58.52	56.50	63.61	61.06	50.40	61.55	60.78
Al_2O_3	26.31	27.88	26.10	21.80	25.56	26.00	27.59	22.83	24.82	31.53	23.90	24.64
FeO	0.25	0.33	0.30	0.41	0.36	0.36	0.31	0.26	0.37	0.30	0.34	0.32
CaO	7.88	9.55	7.83	2.59	7.00	7.65	8.85	3.63	5.71	13.76	5.15	5.80
Na_2O	7.27	5.90	7.04	10.03	7.44	7.08	6.38	9.92	7.99	3.61	8.11	7.87
K_2O	0.34	0.32	0.38	0.43	0.39	0.49	0.27	0.58	0.56	0.11	0.36	0.66
BaO			0.13	0.03	0.12	0.07	0.02	0.09	0.05	0.06		0.01
Total	100.2	99.06	100.1	99.83	100.2	100.4	100.2	101.3	100.8	99.90	99.60	100.4
X_{An}	0.37	0.46	0.37	0.12	0.33	0.36	0.43	0.16	0.27	0.67	0.25	0.28
X_{Ab}	0.61	0.52	0.61	0.85	0.64	0.61	0.56	0.81	0.69	0.32	0.72	0.68
X_{Or}	0.02	0.02	0.02	0.02	0.02	0.03	0.02	0.03	0.03	0.01	0.02	0.04

inc: phase included in Cpx or Amp.
[a] Position represent the relative position of spot analyses within the crystal: int — intermediate between core and border.

Table 6
Microprobe analyses of amphiboles from the Cerro Munro autoliths.

Sample	29b	29b	29b	29b	29b	29b	29b	29b	29b	29b	29b	29b	33a	33a	33a	33a	33a	33a	33a	33a	33a	33a	33a
Position[a]	int	int	int	int	rim	core	rim	core	int	rim	rim	int	core	rim	rim	int	int	int	int	int	core	rim	int
Run	29b1	29b3	29b4	29b11	29b12	29b14	29b17 (inc)	29b21 (inc)	29b22	29b23	29b24 (inc)	29b27	33a1	33a2	33a4	33a5	33a11	33a14	33a15	33a17	33a18	33a19	33a23
SiO_2	49.40	49.11	50.27	50.70	53.84	49.58	49.17	53.84	49.55	52.83	51.18	50.39	53.67	53.88	55.06	47.32	52.30	52.42	52.93	53.06	54.31	52.11	49.06
TiO_2	1.11	1.13	1.25	0.99	0.35	1.35	1.26	0.23	1.49	0.62	0.26	1.04	0.16	0.23	0.06	1.62	0.14	0.33	0.07	0.17	0.29	0.13	1.32
Al_2O_3	4.64	4.85	4.40	4.04	2.08	5.03	5.24	1.50	5.17	2.84	3.86	4.48	1.40	1.75	0.47	5.99	1.27	2.12	1.51	1.33	1.74	1.76	5.29
Cr_2O_3	0.08	0.09	0.01	0.02			0.02	0.00		0.05	0.03	0.13	0.04	0.03	0.09	0.12	0.06	0.11	0.04	0.09			0.05
FeO	14.06	14.35	13.92	14.08	10.70	12.15	14.01	12.14	12.35	11.14	13.50	13.08	14.90	10.57	10.05	14.32	18.11	13.59	16.20	18.71	7.86	15.83	13.07
MnO	0.33	0.31	0.33	0.42	0.51	0.31	0.41	0.43	0.27	0.21	0.41	0.21	0.64	0.30	0.38	0.51	0.66	0.42	0.54	0.70	0.18	0.49	0.30
MgO	15.06	14.74	15.23	15.24	18.14	16.15	14.88	17.45	16.12	17.16	16.12	15.76	14.37	17.67	18.03	14.04	12.16	15.06	14.03	11.74	19.37	14.14	15.77
NiO	0.05		0.01							0.04			0.04	0.08	0.03	0.04	0.00	0.03			0.02	0.03	
CaO	11.06	10.96	10.99	11.08	11.26	11.08	11.16	11.53	11.14	12.12	10.84	11.14	12.16	12.13	12.48	11.15	11.89	12.55	11.53	11.81	12.22	12.04	11.15
Na_2O	1.20	1.46	1.35	1.19	0.58	1.42	1.47	0.35	1.49	0.71	0.96	1.30	0.18	0.40	0.07	1.55	0.25	0.27	0.23	0.24	0.45	0.29	1.49
K_2O	0.41	0.43	0.37	0.33	0.12	0.50	0.47	0.11	0.48	0.23	0.28	0.39	0.07	0.08	0.03	0.54	0.08	0.08	0.07	0.05	0.15	0.10	0.56
F	0.25	0.33	0.40	0.34	0.45	0.55	0.40	0.13	0.25	0.26	0.04	0.25	0.08	0.27		0.58	0.17	0.16		0.03	0.45	0.10	0.67
Total	97.63	97.75	98.53	98.43	98.03	98.12	98.48	97.70	98.29	98.21	97.49	98.17	97.70	97.38	96.73	97.78	97.07	97.13	97.15	97.94	97.03	97.01	98.73
Si (T)[b]	7.18	7.16	7.24	7.30	7.65	7.14	7.12	7.69	7.12	7.52	7.37	7.25	7.81	7.70	7.88	6.98	7.79	7.63	7.76	7.84	7.71	7.65	7.10
Al (T)	0.80	0.83	0.75	0.69	0.35	0.85	0.88	0.25	0.87	0.48	0.63	0.75	0.19	0.30	0.08	1.02	0.21	0.36	0.24	0.16	0.29	0.31	0.90
Ti (T)	0.02	0.01	0.01	0.01	0.00			0.03	0.01	0.00				0.01	0.01			0.01			0.00	0.01	0.00
Ti (C)	0.10	0.12	0.13	0.10	0.03	0.15	0.14		0.15	0.07	0.03	0.11	0.02	0.02		0.18	0.02	0.03	0.01	0.02	0.03		0.14
Al (C)							0.02				0.03	0.01	0.05			0.03	0.01		0.02	0.07			
Cr (C)	0.01	0.01	0.00	0.00			0.00			0.01	0.00	0.01	0.01	0.00	0.01	0.01	0.01	0.01	0.01	0.01			0.01
Fe^{3+} (C)	0.47	0.42	0.41	0.42	0.26	0.41	0.40	0.26	0.41	0.26	0.49	0.40	0.09	0.24	0.10	0.25	0.15	0.24	0.18	0.06	0.21	0.32	0.29
Ni (C)	0.01		0.00							0.01			0.01	0.01	0.00	0.01		0.00			0.00	0.00	
Fe^{2+} (C)	1.15	1.25	1.18	1.20	0.87	0.97	1.24	1.02	0.99	1.02	0.99	1.08	1.72	0.97	1.05	1.43	2.11	1.41	1.72	2.25	0.66	1.59	1.16
Mg (C)	3.27	3.20	3.27	3.27	3.84	3.47	3.21	3.72	3.45	3.64	3.46	3.38	3.12	3.76	3.85	3.09	2.70	3.27	3.07	2.59	4.10	3.09	3.40
Mn^{2+} (B)	0.04	0.04	0.04	0.05	0.06	0.04	0.05	0.05	0.03	0.03	0.05	0.03	0.08	0.04	0.05	0.06	0.07	0.02	0.07	0.08	0.02	0.06	0.04
Fe^{2+} (B)	0.09	0.08	0.08	0.07	0.14	0.08	0.06	0.14	0.08	0.04	0.14	0.09	0.00	0.05	0.03	0.08			0.09		0.06	0.01	0.13
Ca (B)	1.72	1.71	1.70	1.71	1.71	1.71	1.73	1.77	1.71	1.85	1.67	1.72	1.89	1.86	1.91	1.76	1.90	1.96	1.81	1.87	1.86	1.89	1.73
Na (B)	0.15	0.16	0.18	0.17	0.08	0.17	0.16	0.05	0.17	0.08	0.13	0.17	0.03	0.06	0.01	0.09	0.04	0.02	0.03	0.05	0.06	0.04	0.10
Na (A)	0.19	0.25	0.19	0.17	0.08	0.23	0.26	0.05	0.25	0.12	0.13	0.19	0.03	0.06	0.01	0.35	0.04	0.06	0.03	0.02	0.06	0.04	0.32
K (A)	0.08	0.08	0.07	0.06	0.02	0.09	0.09	0.02	0.09	0.04	0.05	0.07	0.01	0.02	0.01	0.10	0.02	0.01	0.01	0.01	0.03	0.02	0.10
OH (W)	1.89	1.85	1.82	1.85	1.80	1.75	1.82	1.94	1.89	1.88	1.98	1.89	1.96	1.88	2.00	1.73	1.92	1.93	2.00	1.99	1.80	1.96	1.70
F (W)	0.11	0.15	0.18	0.15	0.20	0.25	0.18	0.06	0.11	0.12	0.02	0.11	0.04	0.12		0.27	0.08	0.07		0.01	0.20	0.05	0.30
Cl (W)	n.a	n.a	n.a	n.a	n.a	n.a	n.a	n.a	n.a	n.a	n.a	n.a	n.a	n.a	n.a	n.a	n.a	n.a	n.a	n.a	n.a	n.a	n.a
Sum T,C,B,A	15.27	15.33	15.26	15.23	15.10	15.32	15.35	15.07	15.33	15.16	15.19	15.27	15.04	15.07	15.01	15.45	15.05	15.07	15.05	15.03	15.09	15.06	15.42
#Mg	0.72	0.71	0.72	0.72	0.79	0.77	0.71	0.76	0.76	0.77	0.75	0.74	0.64	0.79	0.78	0.67	n.d.	n.d.	0.63	n.d.	0.85	0.66	0.72
P (kbar)[c]	0.60	0.63	0.56	0.51	0.32	0.65	0.69	0.28	0.67	0.38	0.50	0.57	0.27	0.29	0.22	0.85	0.26	0.32	0.28	0.27	0.29	0.30	0.69

Sample	36a	36a	36a	36a	36a	36a	36a	36a	36B	36B	36B	36B	36B	36B	37a	37a	38	38	38	38	38	38	38	38	38	38
Position[a]	core	rim	rim	int	int	rim	core	core	rim	rim	core	int	rim	int	rim	int	int	int	core	rim	int	int	rim	int	int	rim	core
Run	36A10	36A11	36A16	36A32 (inc)	36A38 (inc)	36A40	36A42	36A43 (inc)	36B2	36B4	36B12	36B18	36B19	36B24	37a1	37a14	385	386	387	388	3812	3813	3817	3820	3826	3828	3829
SiO_2	49.35	51.50	51.85	50.05	50.25	49.36	54.59	50.00	46.72	52.52	47.74	47.76	48.80	48.57	53.51	49.78	50.88	49.90	49.77	54.04	47.01	49.25	49.67	49.85	50.28	50.91	49.03
TiO_2	1.16	0.76	0.61	0.76	0.92	1.10	0.29	0.82	1.75	0.67	1.84	1.70	1.45	1.50	0.32	0.93	0.71	0.98	1.01	0.35	1.86	1.27	0.79	1.05	1.03	0.64	1.06
Al_2O_3	4.97	3.51	3.54	4.20	4.13	4.67	1.34	4.55	6.54	2.84	6.63	6.04	5.72	5.52	1.39	3.89	3.72	4.04	4.04	2.02	7.01	4.80	3.98	4.50	4.27	4.02	5.13
Cr_2O_3		0.09		0.06	0.01		0.10	0.10	0.05	0.01	0.06	0.11		0.10		0.10	0.02	0.09	0.05	0.07	0.04	0.07	0.07		0.03		0.00
FeO	13.99	10.60	9.98	14.21	14.95	14.29	9.24	14.24	12.39	8.11	11.48	12.68	12.37	13.13	12.14	14.16	13.94	13.69	14.29	9.43	11.50	12.19	13.83	12.52	13.71	13.49	14.56

MnO	0.30	0.17	0.27	0.31	0.34	0.30	0.21	0.32	0.26	0.13	0.20	0.16	0.26	0.25	0.14	0.38	0.29	0.33	0.37	0.29	0.11	0.22	0.37	0.16	0.27	0.34	0.28
MgO	14.88	17.27	18.05	15.08	15.55	15.41	19.35	15.50	15.76	19.15	16.20	15.32	15.65	15.42	17.01	15.09	15.08	15.17	14.72	18.84	15.55	16.19	15.08	15.77	15.18	15.66	14.28
NiO	0.07		0.07	0.04		0.10			0.01	0.04			0.04		0.05		0.02	0.04	0.05	0.04	0.03	0.04	0.05	0.05	0.09		0.00
CaO	11.01	11.67	11.27	11.03	10.94	10.80	11.73	10.90	11.07	12.12	10.98	11.00	11.19	11.09	11.70	10.90	10.93	10.81	10.81	12.25	10.99	11.02	10.81	11.04	10.91	10.78	10.99
Na_2O	1.20	0.82	0.81	0.90	0.94	1.20	0.45	1.11	1.78	0.71	1.83	1.67	1.54	1.44	0.53	1.38	1.06	1.16	1.13	0.55	1.99	1.36	0.94	1.20	1.14	1.05	1.43
K_2O	0.43	0.36	0.26	0.38	0.36	0.41	0.13	0.37	0.56	0.23	0.52	0.51	0.50	0.49	0.19	0.34	0.27	0.35	0.34	0.12	0.63	0.46	0.30	0.39	0.31	0.29	0.46
F	0.49	0.93	0.65	0.25	0.08	0.43	0.38	0.49	0.55	0.56	0.55	0.85	0.38	0.67	0.77	1.38	0.07	0.22	0.23	0.07	0.16	0.36	0.16	0.04	0.07	0.34	0.15
Total	97.85	97.68	97.36	97.27	98.46	98.06	97.81	98.38	97.43	97.10	98.02	97.79	97.90	98.17	97.74	98.32	96.99	96.78	96.80	98.06	96.87	97.23	96.03	96.57	97.29	97.53	97.37
Si (T)[b]	7.18	7.41	7.42	7.29	7.22	7.14	7.71	7.21	6.82	7.47	6.91	6.99	7.06	7.05	7.71	7.28	7.40	7.27	7.27	7.60	6.89	7.15	7.31	7.26	7.27	7.37	7.18
Al (T)	0.82	0.59	0.58	0.71	0.70	0.80	0.22	0.77	1.13	0.48	1.09	1.01	0.94	0.94	0.24	0.67	0.60	0.69	0.70	0.33	1.11	0.82	0.69	0.74	0.73	0.64	0.83
Ti (T)					0.08	0.06	0.03	0.02	0.05	0.05				0.01	0.03	0.05		0.04	0.03	0.04		0.03			0.00		
Ti (C)	0.13	0.08	0.07	0.08	0.02	0.06		0.07	0.14	0.02	0.20	0.19	0.16	0.15		0.05	0.08	0.07	0.08		0.21	0.11	0.09	0.12	0.11	0.07	0.12
Al (C)	0.03	0.00	0.01	0.01							0.05	0.04	0.04				0.04				0.10		0.00	0.03		0.05	0.06
Cr (C)		0.01		0.01	0.00		0.01	0.01	0.01	0.00	0.01	0.01		0.01		0.01	0.00	0.01	0.01	0.01	0.01	0.01	0.01		0.00		
Fe^{3+} (C)	0.44	0.34	0.39	0.45	0.59	0.60	0.23	0.55	0.51	0.35	0.29	0.26	0.37	0.43	0.22	0.44	0.39	0.61	0.59	0.33	0.22	0.45	0.44	0.40	0.58	0.41	0.38
Ni (C)	0.01		0.01	0.01		0.01			0.00	0.01			0.01		0.01		0.00	0.00	0.01	0.00	0.00	0.01	0.01	0.01	0.01		
Fe^{2+} (C)	1.17	0.87	0.67	1.17	1.06	1.01	0.69	1.04	0.91	0.56	0.97	1.16	1.05	1.07	1.12	1.21	1.22	1.02	1.11	0.71	1.08	0.93	1.14	1.03	1.03	1.09	1.33
Mg (C)	3.23	3.70	3.85	3.27	3.33	3.32	4.07	3.33	3.43	4.06	3.50	3.34	3.38	3.33	3.65	3.29	3.27	3.29	3.20	3.95	3.40	3.50	3.31	3.42	3.27	3.38	3.12
Mn^{2+} (B)	0.04	0.02	0.03	0.04	0.04	0.04	0.03	0.04	0.03	0.02	0.02	0.02	0.03	0.03	0.02	0.05	0.04	0.04	0.05	0.04	0.01	0.03	0.05	0.02	0.03	0.04	0.03
Fe^{2+} (B)	0.09	0.07	0.13	0.12	0.15	0.12	0.14	0.13	0.09	0.06	0.14	0.13	0.07	0.09	0.10	0.08	0.09	0.04	0.04	0.04	0.11	0.10	0.12	0.10	0.05	0.13	0.07
Ca (B)	1.72	1.80	1.73	1.72	1.68	1.68	1.78	1.68	1.73	1.85	1.70	1.73	1.73	1.72	1.81	1.71	1.70	1.69	1.69	1.85	1.72	1.71	1.70	1.72	1.69	1.67	1.72
Na (B)	0.16	0.11	0.11	0.13	0.13	0.17	0.06	0.15	0.14	0.08	0.13	0.12	0.16	0.15	0.07	0.17	0.17	0.23	0.22	0.08	0.15	0.16	0.13	0.16	0.22	0.16	0.17
Na (A)	0.18	0.12	0.11	0.13	0.13	0.17	0.06	0.16	0.36	0.12	0.38	0.35	0.28	0.25	0.08	0.22	0.13	0.10	0.10	0.08	0.42	0.23	0.14	0.18	0.09	0.14	0.24
K (A)	0.08	0.07	0.05	0.07	0.07	0.08	0.02	0.07	0.10	0.04	0.10	0.10	0.09	0.09	0.03	0.06	0.05	0.07	0.06	0.02	0.12	0.09	0.06	0.07	0.06	0.05	0.09
OH (W)	1.77	1.58	1.71	1.88	1.96	1.80	1.83	1.78	1.75	1.75	1.75	1.61	1.83	1.69	1.65	1.36	1.97	1.90	1.89	1.97	1.93	1.83	1.93	1.98	1.97	1.85	1.93
F (W)	0.23	0.42	0.29	0.12	0.04	0.20	0.17	0.23	0.25	0.25	0.25	0.40	0.17	0.31	0.35	0.64	0.03	0.10	0.11	0.03	0.08	0.17	0.07	0.02	0.03	0.16	0.07
Cl (W)	n.a	n.a	n.a	n.a	n.a	n.a	n.a	n.a	n.a	n.a	n.a	n.a	n.a	n.a	n.a	n.a	n.a	n.a	n.a	n.a	n.a	n.a	n.a	n.a	n.a	n.a	n.a
Sum T,C,B,A	15.26	15.19	15.16	15.20	15.20	15.25	15.09	15.22	15.47	15.16	15.48	15.44	15.37	15.34	15.11	15.29	15.18	15.17	15.16	15.10	15.53	15.31	15.19	15.25	15.15	15.19	15.32
#Mg	0.72	0.80	0.83	0.72	0.73	0.75	0.83	0.74	0.77	0.87	0.76	0.72	0.75	0.74	0.75	0.72	0.71	0.76	0.74	0.84	0.74	0.77	0.72	0.75	0.75	0.73	0.69
P (kbar)[c]	0.65	0.45	0.46	0.54	0.53	0.61	0.26	0.59	0.96	0.38	0.96	0.84	0.77	0.74	0.27	0.51	0.48	0.52	0.52	0.31	1.08	0.62	0.52	0.58	0.54	0.51	0.68

inc: phase included in Pl or Fe-Ti oxide.

[a] Position represent the relative position of spot analyses within the crystal: int — intermediate between core and border.

[b] Structural amphibole formula was calculated according to Locock (2014).

[c] Pressure obtained by Amp barometry from Ridolfi et al. (2010).

Table 7
Microprobe analyses of pyroxenes from the Cerro Munro autoliths.

Phase	Cpx	Cpx	Cpx	Cpx	Cpx	Cpx	Cpx	Cpx	Cpx	Cpx	Cpx	Cpx	Cpx	Cpx	Cpx	Cpx	Cpx	Cpx	Cpx	Cpx	Cpx	Cpx	Cpx	Cpx	Opx
Sample	36a	36a	36a	36a	36a	36a	36a	36a	36a	36a	36a	36a	36a	36a	36B	36B	36B	37a	37a	37a	37a	37a	37a	37a	37a
Run	36A-3	36A-13	36A-14	36A-15	36A-22	36A-23	36A-24	36A-25	36A-28	36A-29	36A-30	36A-31	36A-39	36A-47	36B-1	36B-10	36B-11	37a-2	37a-7	37a-10	37a-11	37a-15	37a-19	37a-20	37a-12
Position[a]	inc	core	rim	core	core						core		core, inc	rim, inc	core				inc	core	rim	inc	core	rim	inc
SiO_2	51.29	52.99	51.93	53.11	52.56	52.56	51.96	53.21	53.30	52.58	52.64	52.15	52.43	51.60	51.94	52.64	52.28	53.54	51.97	52.07	53.47	52.82	53.38	52.40	52.70
TiO_2	0.65	0.03	0.16	0.06	0.13	0.10	0.21	0.08	0.09	0.12	0.13	0.21	0.09	0.41	0.21	0.15	0.16	0.06	0.33	0.12	0.05	0.30	0.09	0.21	0.21
Al_2O_3	1.84	0.40	0.74	0.17	0.75	0.14	1.12	0.44	0.37	0.96	0.81	0.94	0.48	1.91	0.78	1.16	0.98	0.34	1.17	0.85	0.33	1.09	0.38	1.11	0.57
Cr_2O_3	0.09	0.01	n.d.	0.10	n.d.	0.01	0.08	0.10	0.02	0.04	0.05	0.06	0.05	0.12	0.10	n.d.	0.16	n.d.	0.03	n.d.	n.d.	n.d.	n.d.	0.09	0.07
FeO	9.50	6.65	10.44	8.32	10.22	10.20	9.92	6.20	6.34	7.99	8.40	9.06	10.02	7.64	8.77	7.06	8.06	7.37	9.41	8.83	7.32	9.49	7.47	9.18	21.86
MnO	0.34	0.22	0.32	0.29	0.35	0.34	0.29	0.27	0.14	0.13	0.31	0.28	0.38	0.21	0.27	0.23	0.35	0.24	0.30	0.30	0.32	0.36	0.27	0.26	0.71
MgO	14.22	15.51	13.95	14.60	13.71	13.59	13.38	15.50	15.45	14.30	14.50	14.68	14.35	15.47	14.90	14.92	15.29	15.05	14.78	14.48	15.53	14.47	15.16	13.88	22.60
NiO	0.11	0.03	0.02	0.06	0.05	0.01	0.10	0.01	n.d.	0.01	0.09	0.04	0.08	0.06	0.03	0.05	0.03	n.d.	0.04	0.07	0.04	n.d.	0.02	n.d.	0.02
CaO	21.07	23.20	21.47	22.95	21.67	22.30	22.06	23.46	23.55	23.09	22.20	21.30	21.66	21.93	21.60	23.04	21.95	22.89	20.90	21.56	22.76	21.30	22.82	22.21	1.09
Na_2O	0.46	0.28	0.28	0.14	0.21	0.13	0.31	0.23	0.23	0.31	0.32	0.26	0.34	0.31	0.40	0.31	0.39	0.28	0.46	0.44	0.31	0.43	0.36	0.50	0.03
K_2O	0.02	0.02	n.d.	0.02	0.01	0.01	n.d.	0.01	0.00	n.d.	n.d.	0.02	0.01	0.01	n.d.	0.01	0.01	0.01	n.d.	0.01	0.01	0.00	0.01	0.00	0.00
F	n.d.	0.03	0.06	n.d.	0.07	n.d.	0.19	n.d.	n.d.	n.d.	0.09	0.24	n.d.	n.d.	0.22	0.02	n.d.	0.11	0.03	0.10	0.03	0.06	n.d.	0.08	n.d.
Total	99.61	99.51	99.38	99.85	99.76	99.40	99.61	99.55	99.55	99.61	99.53	99.26	99.91	99.79	99.27	99.60	99.72	99.98	99.50	98.91	100.16	100.37	99.99	99.96	99.95
#Mg[b]	0.73	0.81	0.70	0.76	0.71	0.70	0.71	0.82	0.81	0.76	0.75	0.74	0.72	0.78	0.75	0.79	0.77	0.78	0.74	0.75	0.79	0.73	0.78	0.73	0.65

Phase	Cpx	Cpx	Cpx	Cpx	Cpx	Opx	Opx	Opx	Opx
Sample	37	38	38	38	38	38	38	38	38
Run	38–1	38–11	38–16	38–22	38–25	38–2	38–15	38–21	38–27
Position[a]	int	relic core		inc		inc		inc	relic core
SiO_2	51.80	53.14	52.42	52.81	52.43	52.56	52.87	53.04	53.60
TiO_2	0.26	0.09	0.35	0.26	0.41	0.23	0.19	0.21	0.14
Al_2O_3	1.10	0.43	1.18	0.87	1.45	0.61	0.66	0.63	0.45
Cr_2O_3	n.d.	0.03	0.13	0.01	0.08	0.01	0.03	0.02	n.d.
FeO	8.80	8.25	9.65	9.02	8.75	23.34	22.76	21.89	21.57
MnO	0.41	0.26	0.29	0.31	0.29	0.84	0.67	0.55	0.57
MgO	14.67	14.15	13.70	14.25	14.56	21.50	21.81	22.28	22.65
NiO	0.01	0.02	0.04	n.d.	0.02	0.04	n.d.	n.d.	0.02
CaO	21.18	22.96	21.73	21.33	21.60	1.11	1.24	1.40	1.13
Na_2O	0.48	0.34	0.43	0.37	0.44	0.03	0.03	0.03	0.03
K_2O	n.d.	0.02	n.d.	n.d.	n.d.	0.00	0.01	0.01	0.02
F	0.07	n.d.	n.d.	0.07	n.d.	n.d.	n.d.	n.d.	0.17
Total	98.82	99.73	99.94	99.33	100.1	100.3	100.3	100.1	100.5
#Mg[b]	0.75	0.75	0.72	0.74	0.75	0.62	0.63	0.64	0.65

inc: phase included in Pl.
n.d.: not determined.
[a] Position represent the relative position of spot analyses within the crystal: inc — inclusion.
[b] Mg# = molar MgO/[MgO + FeO].

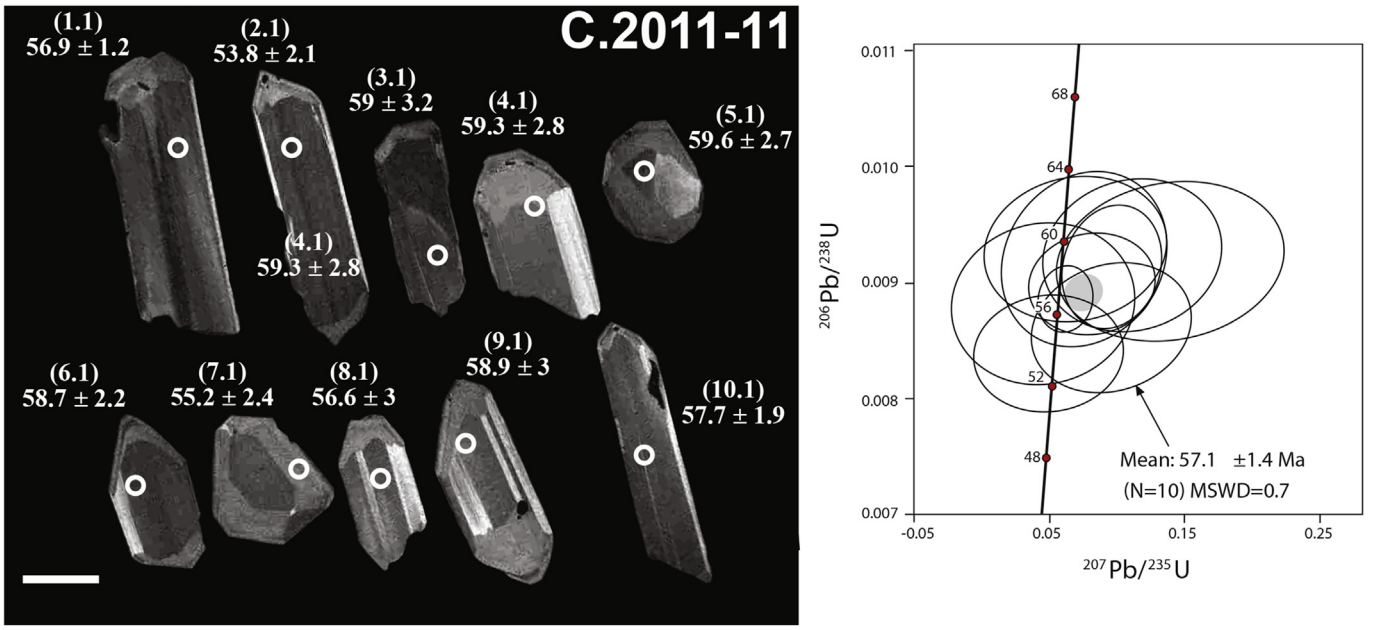

Fig. 10. Cathodoluminiscence images of the analysed zircon sample. Spots location and their resulting $^{206}Pb/^{238}U$ ages (Ma) are indicated. Data are given in Table 8. Scale bars are 100 μm. Concordia U-Pb diagrams for both studied samples are shown beside CL images. Error ellipses for data points in the Concordia diagrams are 68.3% confidence limits, including the error from the standard. Grey ovoids represent the calculated concordia ages.

Table 8
Summary of SHRIMP U-Pb zircon data for Cerro Munro tonalite.

Id	ppm			$\%Pb_c$	Th/U	[a]Isotope ratios						[a]Age (Ma)				[b]Age (Ma)	
	U	Th	^{206}Pb			$^{207}Pb/^{206}Pb$	±%	$^{206}Pb/^{238}U$	±%	$^{207}Pb/^{235}U$	±%	$^{208}Pb/^{232}Th$	±err	$^{206}Pb/^{238}U$	±err	$^{206}Pb/^{238}U$	±err
C.2011-11																	
1.1	169	255	1.35	4.65	1.56	0.052	22	0.0089	2.1	0.063	22	47.1	3.8	56.9	1.2	56.6	1.3
2.1	130	181	1.01	6.85	1.44	0.043	73	0.0084	4	0.050	73	41.9	8.8	53.8	2.1	54.1	1.6
3.1	80	99	0.69	7.67	1.27	0.060	54	0.0092	5.5	0.076	54	53.0	12	59.0	3.2	58.0	2.4
4.1	67	68	0.57	6.70	1.06	0.088	38	0.0092	4.8	0.113	39	60.0	13	59.3	2.8	56.2	2.8
5.1	55	45	0.47	7.39	0.85	0.055	64	0.0093	4.5	0.070	64	63.0	18	59.6	2.7	59.1	2.2
6.1	94	125	0.78	4.78	1.38	0.077	25	0.0091	3.9	0.097	25	61.6	6.1	58.7	2.2	56.5	2.2
7.1	85	87	0.66	4.33	1.06	0.082	40	0.0086	4.3	0.097	40	74.0	13	55.2	2.4	52.8	1.9
8.1	56	61	0.50	15.9	1.13	0.038	98	0.0088	5.3	0.046	98	35.0	13	56.6	3.0	57.3	2.7
9.1	50	55	0.43	8.90	1.14	0.111	39	0.0092	5	0.140	40	75.0	16	58.9	3.0	54.2	2.9
10.1	86	112	0.71	6.86	1.34	0.066	39	0.0090	3.2	0.082	39	52.8	7.4	57.7	1.9	56.3	1.9

Errors are 1-sigma; Pb_c and ^{206}Pb indicate the common and radiogenic portions, respectively.
Error in Standard calibration was 0.31%(not included in above errors but required when comparing data from different mounts).
[a] Common Pb corrected using measured ^{204}Pb.
[b] Common Pb corrected by assuming $^{206}Pb/^{238}U$-$^{207}Pb/^{235}U$ age-concordance.

since zircon crystallization ages gives an homogenous age for the pluton (Fig. 11).

Zoned eruptive (Deering et al., 2011; Hildreth and Wilson, 2007) or intrusive (Bateman and Chappell, 1979; Lee et al., 2015) products are usually found in nature but also it is possible to find this zoning in volcanic and plutonic rocks which are related to each other. The combined study of plutonic bodies and volcanic related rocks can help us validate the hypothesis supported on petrological and geochemical evidences from a fossil magma chamber.

Cumulate features of both tonalites and autoliths from Cerro Munro intrusive body imply the expulsion of a differentiated liquid that can also increase the basicity. At this point, the question is whether the tonalites represent a residue from which a differentiate liquid is extracted. This is predicted by crystallization models within a solidification front, in which the liquid is expelled when the water saturation is reached (Rodríguez and Castro, 2017). The influence of water on the differentiation trend of calc-alkaline series has been broadly discussed (Bachmann and Bergantz, 2004; Kawamoto, 1996; Sisson and Grove, 1993). Here, we propose a crystallization model for the Cerro Munro system, consisting of fractionation by batches induced by the water saturation magma. Both at the sidewalls of a magmatic reservoir and at the ascent conduits, the temperature interval between *solidus* and *liquidus* establishes a solidification front (Marsh, 2002), in which the water saturation will be reached as the crystallization proceeds by second boiling (Burnham, 1979). Cumulate features such as textures and geochemical signatures, can be explained by the presence of a solidification front, from which a residual liquid is expelled. This can potentially trigger a further volcanic event recorded by late rhyolite porphyries, as a consequence of the second boiling, favoured by the extensional tectonic setting. Simple variation diagrams for incompatible elements as SiO_2 vs Rb or Li (Fig. 13) show that these

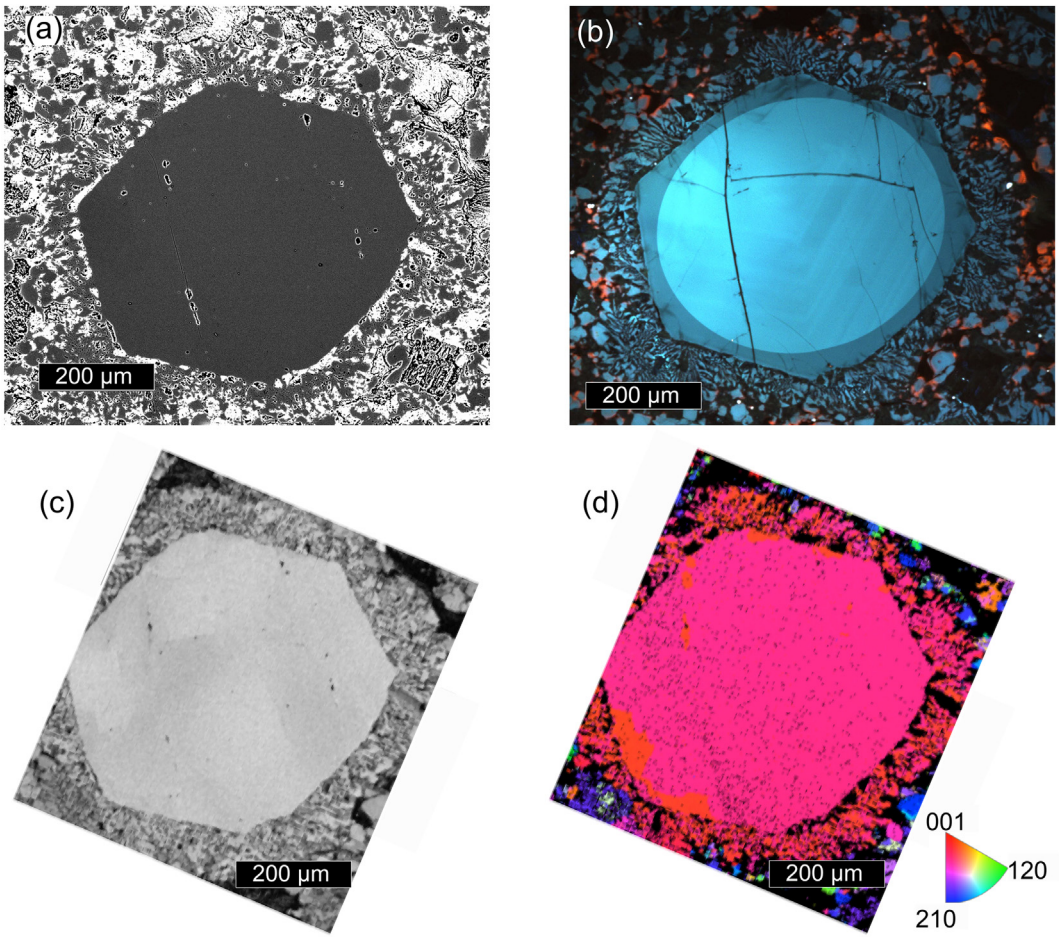

Fig. 11. (a) BSE image of Qz from rhyolitic porphyry A312-24. (b) Real colour cathodoluminiscence image of Qz from sample A312-24. (c) Image quality. (d) Orientation map using Miller indices as orientation parameter. Red colour indicates the occurrence of the *c* crystallographic axis of Qz parallel to the normal direction in the sample (z). A certain grade of misorientation can be appreciated in the idiomorphic crystal of the image. In addition, Qz occurring at the myrmekite rims maintains the orientation of large central crystal. (For interpretation of the references to colour in this figure legend, the reader is referred to the web version of this article.)

differentiated liquids are enriched in soluble elements. From this, we can also deduce that the segregated liquid from this crystal mush was assisted by high water contents. The successive water saturation in a magmatic system can develop different pulses of fractionated magma, giving rise to the differentiation pattern of tonalites and autoliths of Cerro Munro intrusion.

10. Conclusions

The integrated study of plutons and all its related rocks, such as enclaves and dikes, is necessary to reconstruct the tectono-magmatic history of magma chambers. The Cerro Munro tonalite has crystallized according to a modified calc-alkaline pattern at shallow depths of emplacement. The role of water on the differentiation trend of this pluton, as a promoter of the expulsion of different batches of magma, explains the deviation from the traditional calc-alkaline pattern. The analysis of igneous textures reveals the value of the second boiling as a precursor mechanism of the differentiation in calc-alkaline magmas. Petrographical and geochemical tools are essential to take advantage of the information registered in plutonic rocks. Plutonic enclaves are ubiquitous in silicic plutons and can be used to define the relation to the host pluton, which is expected to connect them both with a common magma chamber. The study of volcanic rocks related to the fossil magma chamber supports this fractionation mechanism by batches. The plutonic-volcanic connection is not only evidenced in

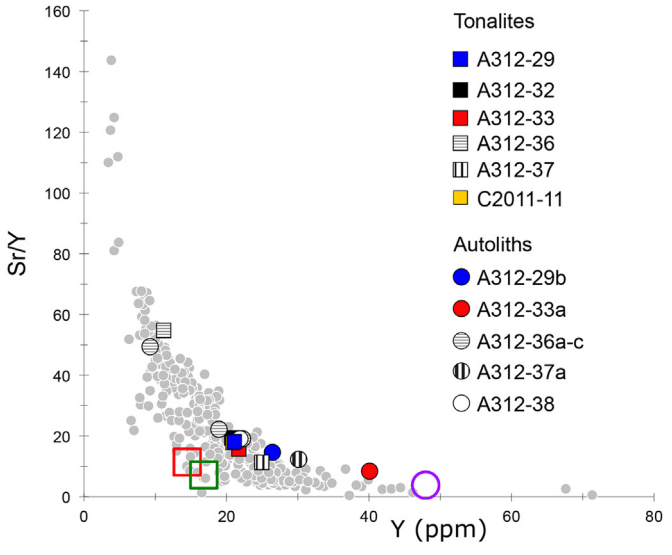

Fig. 12. Sr/Y vs Y diagram showing tonalites and autoliths from Cerro Munro body. Grey dots represent the Peninsular Range batholith (California, USA). Also, experiments from Castro et al. (2010) are included for comparison. Red square represents conditions of 1100 °C and 20 kbar. Green Square corresponds to 1050 °C and 15 kbar and the purple circle represents the melange melting at 1100 °C and 15 kbar. (For interpretation of the references to colour in this figure legend, the reader is referred to the web version of this article.)

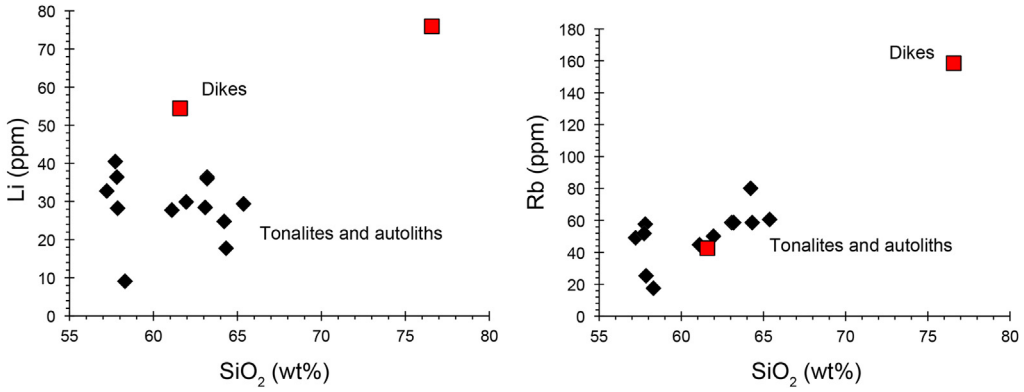

Fig. 13. (a) Li vs SiO_2 diagram for tonalites, autoliths and dikes from Cerro Munro magmatic system. (b) Rb vs SiO_2 diagram showing the geochemical trend for the entire set of tonalites, autoliths and dikes.

the case of the Cerro Munro magmatic system but also contributes to the knowledge about processes governing the cooling and solidification of magmatic systems.

Acknowledgments

This work is supported by MINECO grant LITHOS project CGL2013-48408-C3-1-P. C. R. is grateful for her AUIP grant (Asociación Universitaria Iberoamericana de Postgrado) for the stay at the Universidad Nacional de La Plata (Argentina) and for her postdoctoral contract from the University of Huelva (under the Estrategia Politíca Científica de la UHU 2016/2017).

Appendix A. Supplementary data

Supplementary data related to this article can be found at http://dx.doi.org/10.1016/j.jsames.2017.06.002.

References

Aragón, E., Aguilera, Y., Cavarozzi, C., Ribot, A., 2005. Basaltos Alcalinos en el Complejo Volcánico-Piroclastico del Río Chubut medio. Actas XVI Congr. Geol. Argent. Actas 485–486.
Aragón, E., D'Eramo, F., Castro, A., Pinotti, L., Brunelli, D., Rabbia, O., Rivalenti, G., Varela, R., Spakman, W., Demartis, M., Cavarozzi, C.E., Aguilera, Y.E., Mazzucchelli, M., Ribot, A., 2011. Tectono-magmatic response to major convergence changes in the North Patagonian suprasubduction system; the Paleogene subduction–transcurrent plate margin transition. Tectonophysics 509 (3–4), 218–237.
Aragón, E., Mazzoni, M.M., 1997. Geología y estratigrafía del complejo volcánico piroclástico del río Chubut medio (Eoceno), Chubut. Argent. Rev. Asoc. Geol. Argent. 52 (3), 243–256.
Bachmann, O., Bergantz, G.W., 2004. On the origin of crysytal-poor rhyolites: extracted from batholitic crystal mushes. J. Petrol. 45, 1565–1582.
Bachmann, O., Bergantz, G.W., 2008. Rhyolites and their source mushes across tectonic settings. J. Petrol. 49 (12), 2277–2285.
Bachmann, O., Miller, C.F., de Silva, S.L., 2007. The volcanic–plutonic connection as a stage for understanding crustal magmatism. J. Volcanol. Geotherm. Res. 167 (1–4), 1–23.
Baedecker, P.A., 1987. Methods for Geological Analysis. U.S Geological Survey Bulletin 1770. US Geological Survey Bulletin, p. 187.
Bateman, P.C., Chappell, B.W., 1979. Crystallization, fractionation, and solidification of the tuolumne intrusive series, Yosemite national park, California. Geol. Soc. Am. Bull. 90, 465–482.
Bea, F., Montero, P., Stroh, A., Baasner, J., 1996. Microanalysis of minerals by an Excimer UV-LA-ICP-MS system. Chem. Geol. 133 (1), 145–156.
Beane, R., Wiebe, R.A., 2012. Origin of quartz clusters in Vinalhaven granite and porphyry, coastal Maine. Contrib. Mineral. Petrol. 163 (6), 1069–1082.
Bellos, L.I., Castro, A., Díaz-Alvarado, J., Toselli, A., 2015. Multi-pulse cotectic evolution and in-situ fractionation of calc-alkaline tonalite–granodiorite rocks, Sierra de Velasco batholith, Famatinian belt, Argentina. Gondwana Res. 27 (1), 258–280.
Boggs, S., Kwon, Y.-I., Goles, G.G., Rusk, B.G., Krinsley, D., Seyedolali, A., 2002. Is quartz cathodoluminescence color a reliable provenance Tool? A quantitative examination. J. Sediment. Res. 72 (3), 408–415.
Boudreau, A., 2016. Bubble migration in a compacting crystal-liquid mush. Contrib. Mineral. Petrol. 171 (4), 32.
Burnham, C.W., 1979. The importance of volatile constituents. In: Yoder, H.S.J. (Ed.), The Evolution of the Igneous Rocks. Princeton University Press, Princeton, pp. 439–482.
Castro, A., Gerya, T., García-Casco, A., Fernández, C., Díaz Alvarado, J., Moreno-Ventas, I., Loew, I., 2010. Melting relations of MORB-sediment mélanges in underplated mantle wedge plumes. Implications for the origin of cordilleran-type batholiths. J. Petrol. 51 (6), 1267–1295.
Cazau, L., Mancini, D., Cangini, J., Spallettil, L., 1989. Cuenca Ñirihuau. In: Chebli, G., Spalletti, l. (Eds.), Cuencas Sedimentarias de Argentina, vol. 6. Correlación Geológica, pp. 299–318.
Cumming, G.L., Richards, J.R., 1975. Ore lead isotope ratios in a continuously changing earth. Earth Planet. Sci. Lett. 28 (2), 155–171.
D'Lemos, R.S., Kearsley, A.T., Pembroke, J.W., Watt, G.R., Wright, P., 1997. Complex quartz growth histories in granite revealed by scanning cathodoluminescence techniques. Geol. Mag. 134 (4), 549–552.
Deering, C.D., Bachmann, O., 2010. Trace element indicators of crystal accumulation in Silicic igneous rocks. Earth Planet. Sci. Lett. 297 (1–2), 324–331.
Deering, C.D., Cole, J.W., Vogel, T.A., 2011. Extraction of crystal-poor rhyolite from a hornblende-bearing intermediate mush: a case study of the caldera-forming Matahina eruption, Okataina volcanic complex. Contrib. Mineral. Petrol. 161 (1), 129–151.
Deering, C.D., Keller, B., Schoene, B., Bachmann, O., Beane, R., Ovtcharova, M., 2016. Zircon record of the plutonic-volcanic connection and protracted rhyolite melt evolution. Geology 44, 267–270.
Donev, A., Cisse, I., Sachs, D., Variano, E.A., Stillinger, F.H., Connelly, R., Torquato, S., Chaikin, P.M., 2004. Improving the density of jammed disordered packings using ellipsoids. Science 303 (5660), 990–993.
Frost, C.D., Frost, B.R., Beard, J.S., 2016. On silica-rich granitoids and their eruptive equivalents. Am. Mineral. 101 (6), 1268–1284.
Gelman, S.E., Deering, C.D., Bachmann, O., Huber, C., Gutiérrez, F.J., 2014. Identifying the crystal graveyards remaining after large silicic eruptions. Earth Planet. Sci. Lett. 403, 299–306.
Giacosa, R., Heredia, N., 2004. Structure of the North Patagonian thick-skinned foldand-thrust belt, southern central Andes, Argentina (41°–42° S). J. S. Am. Earth Sci. 18, 61–72.
Glazner, A.F., 2014. Magmatic life at low Reynolds number. Geology 42 (11), 935–938.
Glazner, A.F., Coleman, D.S., Bartley, J.M., 2008. The tenuous connection between high-silica rhyolites and granodiorite plutons. Geology 36 (2), 183–186.
Haller, M.J., Linares, M., Ostera, H.A., Page, S.M., 1999. Petrology and Geochronology of the Sub-cordilleran Plutonic Belt of Patagonia, Argentina, II South American Symposium on Isotope Geology, pp. 210–214. Carlos Paz, Argentina.
Hervé, F., Pankhurst, R.J., Fanning, C.M., Calderon, M., Yaxley, G.M., 2007. The South Patagonian batholith: 150 my of granite magmatism on a plate margin. Lithos 97 (3–4), 373–394.
Hildreth, W., Wilson, C.J.N., 2007. Compositional zoning of the bishop tuff. J. Petrol. 48 (5), 951–999.
Jordan, T.E., Burns, W.M., Veiga, R., Pángaro, F., Copeland, P., Kelley, S., Mpodozis, C., 2001. Extension and basin formation in the southern Andes caused by increased convergence rate: a Mid-Cenozoic trigger for the Andes. Tectonics 20 (3), 308–324.
Kawamoto, T., 1996. Experimental constraints on differentiation and H_2O abundance of calc-alkaline magmas. Earth Planet. Sci. Lett. 144 (3–4), 577–589.
Kay, S.M. and Rapela, C.W., 1987. El volcanismo del Terciario inferior y medio en los Andes Norpatagónicos (40°–42° 30′S): Origen de los magmas y su relación con variaciones en la oblicuidad de la zona de subducción, 10° Congreso Geológico Argentino. Actas, pp. 192–194.
Kirkpatrick, R.J., 1981. Kinetics of crystallization of igneous rocks. Rev. Mineral. 321–395 (United States): Medium: X; Size.

Langmuir, C.H., 1989. Geochemical consequences of In situ crystallization. Nature 340, 199–205.
Leake, B.E., Woolley, A.R., Arps, C.E.S., Birch, W.D., Gilbert, M.C., Grice, J.D., Hawthorne, F.C., Kato, A., Kisch, H.J., Krivovichev, V.G., Linthout, K., Laird, J., Mandarino, J.A., Maresch, W.V., Nickel, E.H., Rock, N.M.S., Schumacher, J.C., Smith, D.C., Stephenson, N.C.N., Ungaretti, L., Whittaker, E.J.W., Youzhi, Guo, 1997. Nomenclature of amphiboles; report of the subcommittee on amphiboles of the international mineralogical association, commission on new minerals and mineral names. Am. Mineral. 82 (9–10), 1019–1037.
Lee, C.-T.A., Morton, D.M., Farner, M.J., Moitra, P., 2015. Field and model constraints on silicic melt segregation by compaction/hindered settling: the role of water and its effect on latent heat release. Am. Mineral. 100 (8–9), 1762–1777.
Lee, C.T.A., Morton, D.M., 2015. High silica granites: terminal porosity and crystal settling in shallow magma chambers. Earth Planet. Sci. Lett. 409, 23–31.
Lipman, P.W., Bachmann, O., 2015. Ignimbrites to batholiths: integrating perspectives from geological, geophysical, and geochronological data. Geosphere 11 (3), 705–743.
Locock, A.J., 2014. An Excel spreadsheet to classify chemical analyses of amphiboles following the IMA 2012 recommendations. Comput. Geosci. 62, 1–11.
Ludwig, K.R., 2003. Mathematical–statistical treatment of data and errors for 230Th/U geochronology. Rev. Mineral. Geochem. 52 (1), 631–656.
Mancini, C.D. and Serna, M.J., 1989. Evaluación petrolera de la cuenca de Ñirihuau, Sudoeste de la Argentina, I Congreso Nacional de Hidrocarburos, pp. 739–762.
Marsh, B.D., 2002. On bimodal differentiation by solidification front instability in basaltic magmas, part 1: basic mechanics. Geochim. Cosmochim Acta 66, 2211–2229.
Matthews, N.E., Huber, C., Pyle, D.M., Smith, V.C., 2012. Timescales of magma recharge and reactivation of large silicic systems from Ti diffusion in quartz. J. Petrol. 53 (7), 1385–1416.
Matthews, N.E., Pyle, D.M., Smith, V.C., Wilson, C.J.N., Huber, C., Hinsberg, V., 2011. Quartz zoning and the pre-eruptive evolution of the ~340-ka Whakamaru magma systems, New Zealand. Contrib. Mineral. Petrol. 163 (1), 87–107.
Muñoz, J., Troncoso, R., Duhart, P., Crignola, P., Farmer, L., Stern, C.R., 2000. The relation of the mid-Tertiary coastal magmatic belt in south-central Chile to the late Oligocene increase in plate convergence rate. Rev. Geol. Chile 27, 177–203.
Naney, M.T., 1983. Phase equilibria of rock-forming ferromagnesian silicates in granitic systems. Am. J. Sci. 283, 993–1033.
Pankhurst, R.J., Weaver, S.D., Hervé, F., Larrondo, P., 1999. Mesozoic-cenozoic evolution of the north patagonian batholith in aysen, southern Chile. J. Geol. Soc. 156 (4), 673–694.
Pistone, M., Arzilli, F., Dobson, K.J., Cordonnier, B., Reusser, E., Ulmer, P., Marone, F., Whittington, A.G., Mancini, L., Fife, J.L., Blundy, J.D., 2015. Gas-driven filter pressing in magmas: insights into in-situ melt segregation from crystal mushes. Geology 43 (8), 699–702.
Ramseyer, K., Baumann, J., Matter, A., Mullis, J., 1988. Cathodoluminescence colours of a-quartz. Am. Mineral. 52, 669–677.
Ramseyer, K., Mullis, J., 1990. Factors influencing short-lived blue cathodoluminescence of a-quartz. Am. Mineral. 75, 791–800.
Ramseyer, K., Mullis, J., 2000. Geologic application of cathodoluminescence of silicates. In: Pagel, M., Barbin, V., Blanc, P., Ohnenstetter, D. (Eds.), Cathodoluminescence in Geosciences. Springer Berlin Heidelberg, Berlin, Heidelberg, pp. 177–191.
Rapela, C.W., Pankhurst, R.J., Fanning, C.M., Hervé, F., 2005. Pacific subduction Coeval with the Karoo Mantle Plume: the Early Jurassic Subcordilleran Belt of Northwestern Patagonia. Geological Society Special Publication, pp. 217–239.
Rapela, C.W., Spalletti, l., Merodio, J.C., Aragón, E., 1987. Temporal evolution and spatial variation of the lower tertiary Andean volcanism (40-42 30'S). J. S. Am. Earth Sci. 1, 1–14.
Rapela, C.W., Spalletti, L., Merodio, J.C., 1983. Evolución magmática y geotectónica de la Serie Andesitica andina (Paleoceno–Eoceno) en la cordillera norpatagónica. Rev. Asoc. Geol. Argent. 38 (3–4), 469–484.
Ridolfi, F., Renzulli, A., Puerini, M., 2010. Stability and chemical equilibrium of amphibole in calc-alkaline magmas: an overview, new thermobarometric formulations and application to subduction-related volcanoes. Contrib. Mineral. Petrol. 160 (1), 45–66.
Rodríguez, C., Castro, A., 2017. Silicic magma differentiation in ascent conduits. Experimental constraints. Lithos 272–273, 261–277.
Scaillet, B., Evans, B.W., 1999. The 15 June 1991 eruption of Mount Pinatubo. I. Phase equilibria and pre-eruption P-T-fO2-fH2O conditions of the dacite magma. J. Petrol. 40 (3), 381–411.
Silvestro, J., Zubiri, M., 2008. Convergencia oblicua: modelo estructural alternativo para la dorsal Neuquina (39°S)- Neuquén. Rev. Asoc. Geol. Argent. 63 (1), 49–64.
Sisson, T.W., Grove, T.L., 1993. Experimental investigations of the role of H2O in calc-alkaline differentiation and subduction zone magmatism. Contrib. Mineral. Petrol. 113 (2), 143–166.
Spalletti, L.A., 1983. Paleogeografía de la Formación Ñirihuau y sus equivalentes en la región occidental de Neuquén, Río Negro y Chubut. Rev. Asoc. Geol. Argent. 38 (3–4), 454–468.
Spikermann, J.P., 1978. Contribución al conocimiento de la intrusividad en el Paleozoico de la región extraandina del Chubut. Rev. Asoc. Geol. Argent. 33 (1).
Spikermann, J.P., Sterlin, J., Marshall, P., Carrillo, R., Montenegro, T., Lago, M., Villalba, E., Perez, A., 1988. Geología del área del batolito Aleusco, Departamento de Languiñeo, Provincia de Chubut. Rev. Asoc. Argent. Mineral. Petrol. Sedimentol. 19 (1/4), 39–48.
Spikermann, J.P., Sterlin, J., Marshall, P., Carrillo, R., Montenegro, T., Lago, M., Villalba, E., Perez, A., 1989. Caracterización geologica y petrologica del batolito Aleusco, Departamento de Languiñeo, Provincia de Chubut. Rev. Asoc. Argent. Mineral. Petrol. Sedimentol. 20 (1/4), 33–42.
Steiger, R.H., Jäger, E., 1977. Subcommission on geochronology: convention on the use of decay constants in geo- and cosmochronology. Earth Planet. Sci. Lett. 36 (3), 359–362.
Sun, S.s., McDonough, W.F., 1989. Chemical and isotopic systematics of oceanic basalts: implications for mantle composition and processes. Geol. Soc. Lond. Spec. Publ. 42 (1), 313–345.
Sunagawa, I., 1981. Characteristics of crystal growth in nature as seen from the morphology of mineral crystals. Bull. Mineral. 104, 81–87.
Turner, J.S., 1982. Descripción Geológica de la Hoja 44c. Servicio Geológico Nacional Boletín, Tecka, Provincia de Chubut, 180 92.
Vernon, R.H., Collins, W.J., 2011. Structural criteria for identifying granitic cumulates. J. Geol. 119 (2), 127–142.
Whitney, D.L., Evans, B.W., 2010. Abbreviations for names of rock-forming minerals. Am. Mineral. 95 (1), 185–187.
Wiebe, R.A., Wark, D.A., Hawkins, D.P., 2007. Insights from quartz cathodoluminescence zoning into crystallization of the Vinalhaven granite, coastal Maine. Contrib. Mineral. Petrol. 154 (4), 439–453.
Williams, I.S., 1998. U-Th-Pb geochronology by ion microprobe. In: McKibben, M.A., Shanks III, W.C., Ridley, W.I. (Eds.), Applications of Microanalytical Techniques to Understanding Mineralizing Processes. Reviews in Economic Geology, pp. 1–35.